

# Distinct Effects of Heparin and Interleukin-4 Functionalization on Macrophage Polarization and In Situ Arterial Tissue Regeneration Using Resorbable Supramolecular Vascular Grafts in Rats

**Citation for published version (APA):**

Bonito, V., Koch, S. E., Krebber, M. M., Carvajal-Berrio, D. A., Marzi, J., Duijvelshoff, R., Lurier, E. B., Buscone, S., Dekker, S., de Jong, S. M. J., Mes, T., Vaessen, K. R. D., Brauchle, E. M., Bosman, A. W., Schenke-Layland, K., Verhaar, M. C., Dankers, P. Y. W., Smits, A. I. P. M., & Bouten, C. V. C. (2021). Distinct Effects of Heparin and Interleukin-4 Functionalization on Macrophage Polarization and In Situ Arterial Tissue Regeneration Using Resorbable Supramolecular Vascular Grafts in Rats. *Advanced Healthcare Materials*, 10(21), Article e2101103. Advance online publication. <https://doi.org/10.1002/adhm.202101103>

**Document license:**  
CC BY-NC-ND

**DOI:**  
[10.1002/adhm.202101103](https://doi.org/10.1002/adhm.202101103)

**Document status and date:**  
Published: 03/11/2021

**Document Version:**  
Publisher's PDF, also known as Version of Record (includes final page, issue and volume numbers)

**Please check the document version of this publication:**

- A submitted manuscript is the version of the article upon submission and before peer-review. There can be important differences between the submitted version and the official published version of record. People interested in the research are advised to contact the author for the final version of the publication, or visit the DOI to the publisher's website.
- The final author version and the galley proof are versions of the publication after peer review.
- The final published version features the final layout of the paper including the volume, issue and page numbers.

[Link to publication](#)

**General rights**

Copyright and moral rights for the publications made accessible in the public portal are retained by the authors and/or other copyright owners and it is a condition of accessing publications that users recognise and abide by the legal requirements associated with these rights.

- Users may download and print one copy of any publication from the public portal for the purpose of private study or research.
- You may not further distribute the material or use it for any profit-making activity or commercial gain
- You may freely distribute the URL identifying the publication in the public portal.

If the publication is distributed under the terms of Article 25fa of the Dutch Copyright Act, indicated by the "Taverne" license above, please follow below link for the End User Agreement:

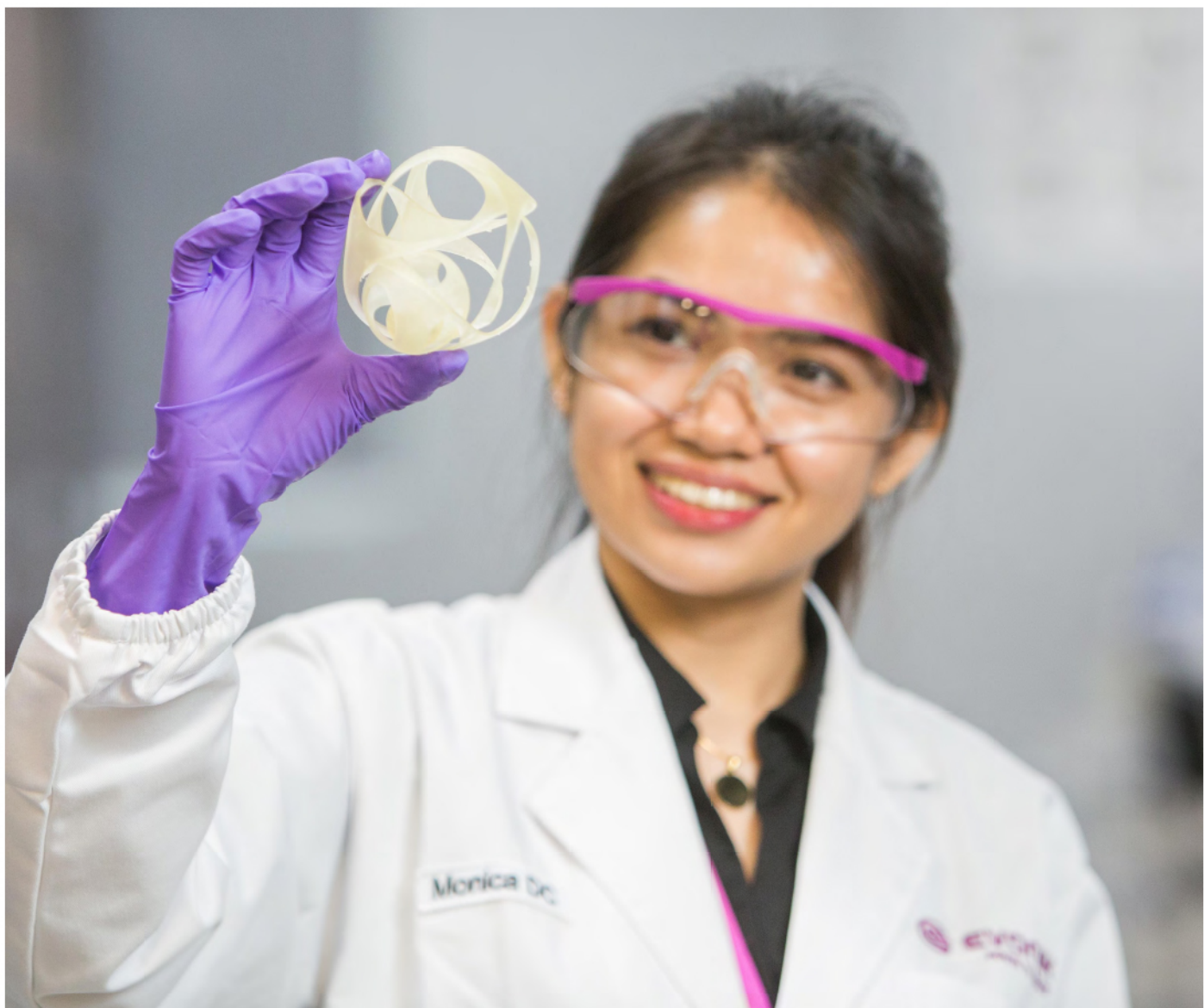
[www.tue.nl/taverne](http://www.tue.nl/taverne)

**Take down policy**

If you believe that this document breaches copyright please contact us at:

[openaccess@tue.nl](mailto:openaccess@tue.nl)

providing details and we will investigate your claim.



Pushing the boundaries  
of chemistry?  
It takes  
#HumanChemistry

Make your curiosity and talent as a chemist matter to the world with a specialty chemicals leader. Together, we combine cutting-edge science with engineering expertise to create solutions that answer real-world problems. Find out how our approach to technology creates more opportunities for growth, and see what chemistry can do for you at:

[evonik.com/career](https://www.evonik.com/career)



# Distinct Effects of Heparin and Interleukin-4 Functionalization on Macrophage Polarization and In Situ Arterial Tissue Regeneration Using Resorbable Supramolecular Vascular Grafts in Rats

Valentina Bonito, Suzanne E. Koch, Merle M. Krebber, Daniel A. Carvajal-Berrio, Julia Marzi, Renee Duijvelshoff, Emily B. Lurier, Serena Buscone, Sylvia Dekker, Simone M. J. de Jong, Tristan Mes, Koen R. D. Vaessen, Eva M. Brauchle, Anton W. Bosman, Katja Schenke-Layland, Marianne C. Verhaar, Patricia Y. W. Dankers, Anthal I. P. M. Smits,\* and Carlijn V. C. Bouten\*

Two of the greatest challenges for successful application of small-diameter in situ tissue-engineered vascular grafts are 1) preventing thrombus formation and 2) harnessing the inflammatory response to the graft to guide functional tissue regeneration. This study evaluates the in vivo performance of electrospun resorbable elastomeric vascular grafts, dual-functionalized with anti-thrombogenic heparin (hep) and anti-inflammatory interleukin 4 (IL-4) using a supramolecular approach. The regenerative capacity of IL-4/hep, hep-only, and bare grafts is investigated as interposition graft in the rat abdominal aorta, with follow-up at key timepoints in the healing cascade (1, 3, 7 days, and 3 months). Routine analyses are augmented with Raman microspectroscopy, in order to acquire the local molecular fingerprints of the resorbing scaffold and developing tissue. Thrombosis is found not to be a confounding factor in any of the groups. Hep-only-functionalized grafts resulted in adverse tissue remodeling, with cases of local intimal hyperplasia. This is negated with the addition of IL-4, which promoted M2 macrophage polarization and more mature neotissue formation. This study shows that with bioactive functionalization, the early inflammatory response can be modulated and affect the composition of neotissue. Nevertheless, variability between graft outcomes is observed within each group, warranting further evaluation in light of clinical translation.

## 1. Introduction

Synthetic vascular grafts are used as vascular replacements for a wide range of clinical conditions, such as atherosclerosis and congenital malformations.<sup>[1]</sup> Even though autologous grafts from saphenous vein or internal thoracic artery remain the golden standard replacement option, limited availability due to the patients' pathophysiological state, and the high long-term failure rates, warrant the development of alternative strategies.<sup>[2-4]</sup> For small diameter (<6 mm) vessel replacements, the current non-biodegradable synthetic grafts (e.g., expanded polytetrafluoroethylene (ePTFE), polyethylene terephthalate (PET)) function inadequately due to the risk of surface thrombogenicity and intimal hyperplasia.<sup>[5-8]</sup> In addition, non-biodegradable grafts lack the ability to repair and remodel the tissue. Tissue-engineered vascular grafts (TEVGs) constructed from biodegradable scaffolds have the potential to overcome these limitations, providing growth capacity and self-repair in situ.<sup>[9-12]</sup>

The ORCID identification number(s) for the author(s) of this article can be found under <https://doi.org/10.1002/adhm.202101103>

© 2021 The Authors. Advanced Healthcare Materials published by Wiley-VCH GmbH. This is an open access article under the terms of the Creative Commons Attribution-NonCommercial-NoDerivs License, which permits use and distribution in any medium, provided the original work is properly cited, the use is non-commercial and no modifications or adaptations are made.

DOI: 10.1002/adhm.202101103

V. Bonito, S. E. Koch, R. Duijvelshoff, E. B. Lurier, S. Buscone, S. Dekker, S. M. J. de Jong, P. Y. W. Dankers, A. I. P. M. Smits, C. V. C. Bouten  
Department of Biomedical Engineering and Institute for Complex Molecular Systems (ICMS)  
Eindhoven University of Technology  
Eindhoven 5600 MB, The Netherlands  
E-mail: a.i.p.m.smits@tue.nl; c.v.c.bouten@tue.nl  
M. M. Krebber, M. C. Verhaar  
Department of Nephrology and Hypertension  
University Medical Center Utrecht  
Utrecht 3584 CX, The Netherlands

The in situ tissue engineering paradigm is based on the exploitation of the inflammatory response, which inevitably occurs upon implantation of the graft. It is acknowledged that the stages of in situ regeneration mirror the phases of the natural wound healing response.<sup>[13]</sup> Implantation of the graft ignites an inflammatory phase that is characterized by the influx of immune cells (i.e., neutrophils and macrophages) and the formation of a preliminary matrix. This is followed by the proliferative phase in which both immune (macrophages and lymphocytes) and tissue producing cells (i.e., stem/progenitor cells and fibroblasts) infiltrate the graft. Next, extracellular matrix (ECM) is deposited and re-endothelization takes place. During the final remodeling phase, the newly formed ECM is remodeled into a functional organization, after which inflammation is resolved and tissue homeostasis is reached upon complete resorption of the scaffold.<sup>[13]</sup>

Two of the greatest challenges for successful application of small-diameter in situ TEVGs are 1) preventing thrombus formation and 2) to prevent adverse remodeling events such as intimal hyperplasia or aneurysm formation.<sup>[7,14,15]</sup> Regarding the latter, macrophages have been demonstrated to be essential cellular modulators of the in situ vascular tissue engineering process.<sup>[16–18]</sup> Depending on their polarization state macrophages accelerate scaffold breakdown on the one hand, and coordinate tissue formation in cross-talk with tissue producing cells (e.g., fibroblasts and smooth muscle cells) on the other hand. Uncoordinated cross-talk as a consequence of a deranged macrophage response will lead to adverse remodeling events like intimal hyperplasia formation.<sup>[19–21]</sup> Accordingly, the macrophage phenotype has been indicated as the predictor for downstream tissue formation.<sup>[22]</sup>

In order to address these challenges, we recently developed a modular functionalization strategy to dual-functionalize electrospun scaffolds with anti-thrombogenic heparin (hep) and anti-inflammatory interleukin-4 (IL-4), based on supramolecular

chemistry.<sup>[23]</sup> IL-4 signaling by T-helper 2 (T<sub>H</sub>2) cells is an important pathway to direct macrophages into a pro-regenerative phenotype (M2) at the onset of wound healing.<sup>[24,25]</sup> Using in vitro 2D and 3D models, we demonstrated the ability of the dual-functionalized material to retain both hep and IL-4 and demonstrated the effective immunomodulatory properties of this novel material.<sup>[23]</sup> Tubular, small-diameter scaffolds were manufactured from a supramolecular elastomer consisting of ureidopyrimidinone (UPy)-modified chain-extended polycaprolactone (CE-UPy-PCL), which was functionalized with a UPy-modified heparin binding peptide (UPy-HBP) to immobilize hep on its surface. Subsequently, the material could be functionalized with IL-4 via its heparin binding domain.<sup>[26,27]</sup>

In the present study, the potential of this novel material approach was evaluated in a long-term in vivo environment, in terms of macrophage modulation and tissue regeneration, while globally screening for thrombosis. To that end, the grafts were implanted for 1, 3 and 7 days and 3 months as interposition grafts in the abdominal aorta of rats. Specifically, we evaluated the effect of functionalization on early macrophage polarization and downstream tissue formation in vivo via histology, mechanical tests with uniaxial tensile tests and scaffold degradation via scanning electron microscopy (SEM). Raman microspectroscopy was used to characterize the biomolecular composition of the grafts radially throughout the vascular graft wall.<sup>[28–30]</sup> This uniquely enabled combined spatial molecular information of de novo ECM formation and scaffold resorption; two of the key processes for in situ tissue engineering. We hypothesized that the modulation of the early macrophage response using IL-4 would lead to an improved tissue formation and prevention of adverse remodeling at later stages, whilst maintaining the beneficial anti-thrombogenic effects of hep.

## 2. Results

### 2.1. Supramolecular Vascular Graft Preparation and Functionalization

Vascular grafts were electrospun from a newly designed supramolecular polymer that allowed for IL-4 functionalization after the electrospinning process.<sup>[23]</sup> First, CE-UPy-PCL was mixed with UPy-HBP (**Figure 1A**). After the UPy-UPy stacking by mixing the CE-UPy-PCL and UPy-HBP solutions (**Figure 1B**), the polymer solution was electrospun into tubular scaffolds with an inner diameter of 2 mm and an average wall thickness of  $284.4 \mu\text{m} \pm 18.7 \mu\text{m}$ . The orientation of the fibers and the average fiber diameter were determined via SEM analysis and showed an isotropic network of interconnected fibers with an average fiber diameter of  $4.84 \mu\text{m} \pm 1.35 \mu\text{m}$  (**Table 1** and **Figure 1C**). The scaffolds were cut to 8 mm in length and were shielded on both ends with an impenetrably dense ( $<1 \mu\text{m}$  internodal distance) Gore-Tex strip of  $4 \times 10 \text{ mm}^2$ , to prevent anastomotic ingrowth (**Figure 1D**), as previously validated and described in detail.<sup>[18]</sup> The suture retention strength of the electrospun tubes with and without GoreTex shielding were both almost sixfold higher than the suture retention strength of the rat abdominal aorta and met the standardized suture retention strength threshold (2 N) for clinical grafts (ISO 7198:2016) (**Figure 1E**). Functionalization occurred according to the design of the three experimental groups: i) the

D. A. Carvajal-Berrio, J. Marzi, E. M. Brauchle, K. Schenke-Layland  
Department of Biomedical Engineering  
Research Institute of Women's Health and Cluster of Excellence iFIT (EXC 2180) "Image-Guided and Functionally Instructed Tumor Therapies"  
Eberhard Karls University Tübingen  
Tübingen 72076, Germany

D. A. Carvajal-Berrio, J. Marzi, E. M. Brauchle, K. Schenke-Layland  
NMI Natural and Medical Sciences Institute at the University of Tübingen  
Reutlingen 72770, Germany

R. Duijvelshoff  
Department of Cardiology  
Isala Hospital  
van Heesweg 2, Zwolle 8025 AB, The Netherlands

E. B. Lurier  
School of Biomedical Engineering  
Science and Health Systems  
Drexel University  
Philadelphia, PA 19104, USA

T. Mes, A. W. Bosman  
SupraPolix BV  
Eindhoven 5612 AX, The Netherlands

K. R. D. Vaessen  
Central Laboratory Animal Research Facility (CLARF)  
Utrecht University  
Utrecht 3584 CX, The Netherlands

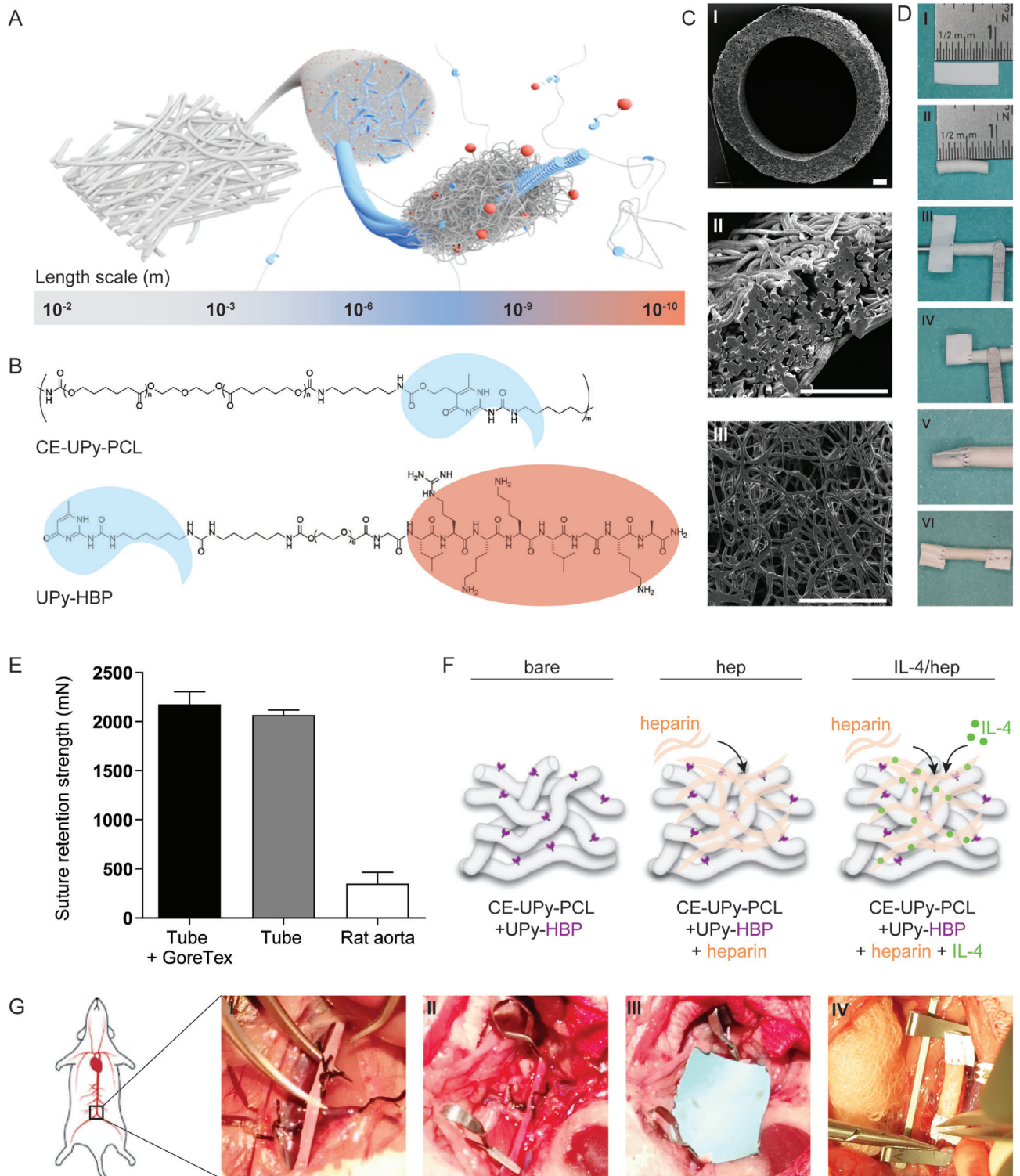


**Figure 1.** Experimental layout and scaffold characterization. A) Schematic representation of self-assembly in supramolecular chain-extended UPy-polymers (CE-UPy-PCL) containing UPy-bioactives. B) Chemical structures of supramolecular elastomer CE-UPy-PCL and the UPy-modified heparin binding peptide (UPy-HBP). C) SEM images of cross sections (I and II) and outer surface (III) of electrospun CE-UPy-PCL+UPy-HBP grafts. Scale bars 200  $\mu$ m. D) Electrospun tubes were cut to 8 mm in length and at both anastomotic sides sutured to a  $4 \times 10$  mm<sup>2</sup> impenetrable Gore-Tex strip. E) Suture retention strength of the electrospun tubes with and without the Gore-Tex strip versus native rat abdominal aorta. F) Schematic representation of the functionalization groups. G) Surgical procedure of graft implantation in abdominal aorta. Panel (A): Adapted from,<sup>[39]</sup> Copyright 2020. Courtesy of ICMS animation studio. Data for suture retention strength presented as mean  $\pm$  SD,  $n = 3$  per group. Abbreviations: ureido-pyrimidinone (UPy), chain-extended (CE), polycaprolactone (PCL), UPy-modified heparin binding peptide (UPy-HBP), heparin (hep), and interleukin (IL).

**Table 1.** Baseline characteristics in vivo study procedure and outcome.

|   |              | Bare              | Hep                  | IL-4/Hep             |
|---|--------------|-------------------|----------------------|----------------------|
| Weight animal (g)   |              | 359 ± 11.0        | 348 ± 15.1           | 354 ± 18.7           |
| Ischemia time implantation procedure (min)                  |              | 56 ± 7            | 59 ± 9               | 54 ± 5               |
| Absolute number of animals analyzed per timepoint per group | 1 days       | 6/7 <sup>a)</sup> | 5/7 <sup>a),c)</sup> | 7/7                  |
|   | 3 days       | 5/7 <sup>b)</sup> | 6/7 <sup>d)</sup>    | 5/7 <sup>b),e)</sup> |
|   | 7 days       | 6/7 <sup>c)</sup> | 6/7 <sup>b)</sup>    | 6/7 <sup>f)</sup>    |
|   | 3 months     | 5/7 <sup>a)</sup> | 5/7 <sup>b)</sup>    | 5/7 <sup>a),e)</sup> |
| Occluded lumen upon gross morphology inspection             | 1 days       | 0/6               | 0/5                  | 1/7 <sup>#</sup>     |
|   | 3 days       | 0/6               | 0/6                  | 0/5                  |
|   | 7 days       | 0/6               | 0/6                  | 0/6                  |
|   | 3 months     | 1/5 <sup>*</sup>  | 1/5 <sup>*</sup>     | 1/5 <sup>*</sup>     |
| Lumen diameter (µm)   | 1 days       | 1824 (±63)        | 1843 (±91)           | 1797 (±54)           |
|   | 3 days       | 1788 (±336)       | 1776 (±162)          | 1780 (±86)           |
|   | 7 days       | 1975 (±116)       | 1852 (±152)          | 1972 (±115)          |
|   | 3 months     | 2303 (±583)       | 2131 (±512)          | 2109 (±229)          |
|   | pre-implant  | 2000 (±49)        |                      |                      |
|   | native aorta | 1101 (±271)       |                      |                      |
| Wall thickness (µm)   | 1 days       | 367 (±52)         | 334 (±50)            | 283 (±38)            |
|   | 3 days       | 329 (±68)         | 403 (±126)           | 390 (±84)            |
|   | 7 days       | 351 (±49)         | 321 (±73)            | 317 (±89)            |
|   | 3 months     | 416 (±78)         | 523 (±105)           | 537 (±118)           |
|   | pre-implant  | 284 (±19)         |                      |                      |
|   | native aorta | 196 (±60)         |                      |                      |

<sup>a-f)</sup> Reason for dropout. Complications during surgery; <sup>a)</sup> Excessive bleeding; <sup>b)</sup> Complications surgical process (e.g., cuts, overdose isoflurane); <sup>c)</sup> Death by unknown cause; <sup>d)</sup> Coagulation issues directly after release of the clamps. Complications postsurgery; <sup>e)</sup> Paralysis paws; <sup>f)</sup> Death by unknown cause. Occlusion: <sup>#</sup> clot; <sup>\*</sup> excess luminal tissue deposition. Abbreviations: interleukin (IL) and heparin (hep).

IL-4/heparin (IL-4/hep group), ii) the heparin only- (hep group), and iii) bare grafts (bare group), the latter which consist of CE-UPy-PCL+UPy-HBP without heparin or IL-4 functionalization (Figure 1F).

## 2.2. Baseline Characteristics Animals and In Vivo Functionality

Baseline characteristics of the animals included in the study, and the absolute animals analyzed are listed (Table 1). The average ischemia time (Figure 1G) was below the intended 60 min and did not differ between experimental groups. To evaluate the early inflammatory response, explants were taken at 1, 3 and 7 days, and to evaluate downstream tissue deposition, explants were taken at 3 months. In total,  $n = 7$  allocated animals per experimental group (bare, hep and IL-4/hep) per timepoint were implanted, and finally 67 grafts were analyzed. The drop out of  $n = 17$  animals in total was not related to the graft type and was due to non-graft related complications due to the microsurgical procedure, as specified in Table 1.

All analyzed grafts allowed for proper hind limb perfusion up to 3 months, with no signs of aneurysm formation nor rupture at the anastomotic sites. At explanation, gross morphology analysis of a sample from the middle part of the explanted graft (Figure S1, Supporting Information; part C) showed that 63/67 grafts were patent, with 1 case of thrombus formation at day 1 in the IL-4/hep group, and 1 out of 5 grafts in all groups at 3 months showing

excess tissue deposition occluding the lumen, regardless of the functionalization of the graft (Table 1; Figure S2D, Supporting Information). The average wall thickness in the middle of the graft showed that the graft wall increased in thickness directly upon implantation. The wall thickness remained the same at the early timepoints, and increased at 3 months for the hep and IL-4/hep group (Figure S2G, Supporting Information). The thickening of the graft wall directly upon implantation is reflected in the slightly lower lumen diameter compared to the pre-implant diameter directly at day 1. The lumen diameter remained constant for the experimental groups at this location in the middle of the graft, except for the bare group, in which an increase in diameter was observed between day 1 and day 3 versus 3 months (Figure S2H, Supporting Information). As can be observed, there was some variation between the animals belonging to one experimental group within one timepoint for both wall thickness and lumen diameter.

## 2.3. Early Host Response

While thrombus formation was not observed in 66/67 analyzed grafts in the gross morphological and functional analysis, SEM analysis of the explants displayed abundant platelet deposition and fibrin network formation at the early time points, in all experimental groups (Figure S3, Supporting Information). At day 1, regardless of functionalization, small fragments as well as

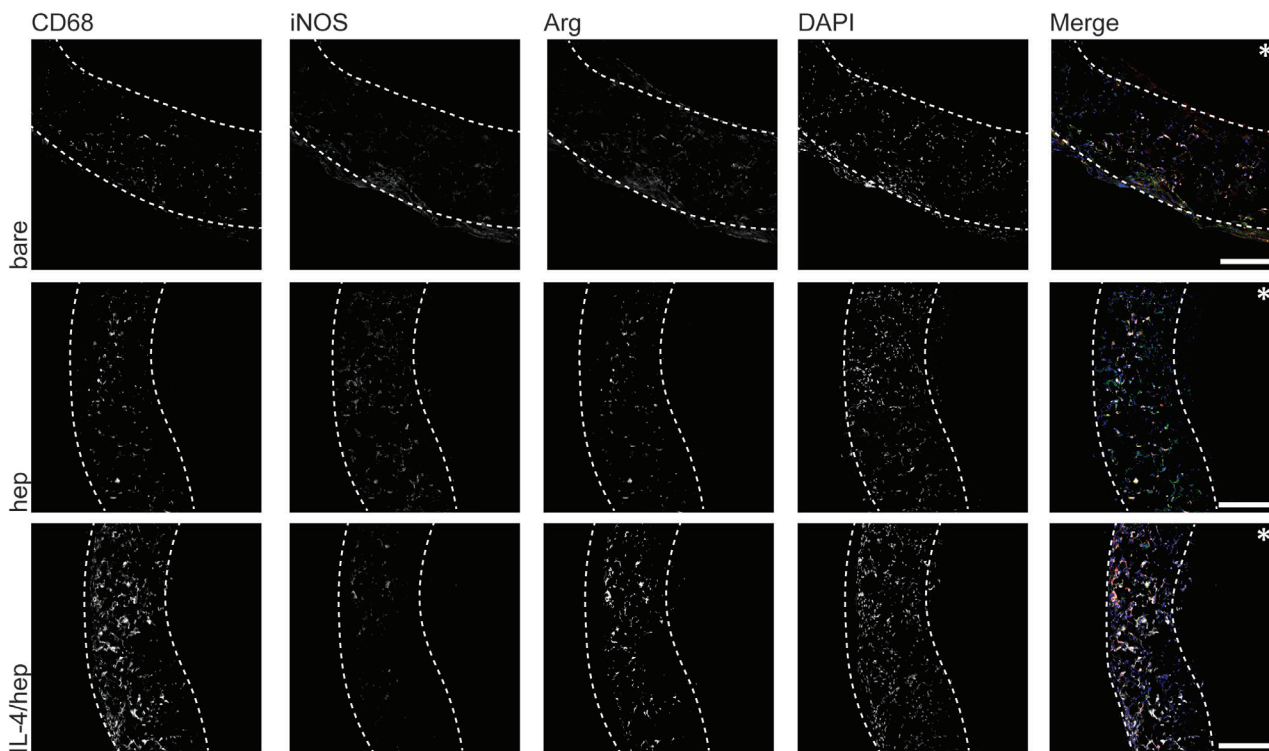


**Figure 2.** Macrophage infiltration and phenotype at day 7. Representative immunofluorescent staining of explants of all experimental groups (bare, hep, IL-4/hep) at day 7. Gray scale images and overlay of pan macrophage marker CD68 (white); M1 marker iNOS (green); M2 marker Arg (red) and cell nuclei DAPI (blue). For day 1, 3 and 3 month timepoint of all experimental groups, see Figure S4 (Supporting Information). Abbreviations: inducible nitric oxide synthase (iNOS), arginase (Arg), heparin (hep), and interleukin (IL). \*Identifies the lumen. Scale bar 150  $\mu\text{m}$ . Dashed lines indicate boundaries of the scaffold.

star-shaped cells were identified, which resembled the morphology of resting and activated platelets, respectively. Additionally, a clear fibrin network was observed in all the experimental groups at day 1 and day 3.

#### 2.4. Heparin and IL-4/Heparin Functionalization Influence Macrophage Recruitment and Polarization

All grafts underwent extensive cellularization within the first week of implantation, followed by tissue formation throughout the grafts. The efficacy of the IL-4/hep functionalization was evaluated in terms of overall infiltration of macrophages and macrophage polarization via immunofluorescence staining of the pan macrophage marker (CD68), M1-marker inducible nitric oxide synthase (iNOS) and M2-marker arginase-1 (Arg) on explants of day 7 (Figure 2) and day 1, 3 and 3 months (Figure S4, Supporting Information). At day 1, there tended to be a slightly reduced influx of CD68<sup>+</sup> macrophages in the hep group, when compared to the other groups (Figures S4A and S5, Supporting Information). Generally, macrophages at day 1 expressed the M1-marker iNOS in all groups. At day 3, the bare group showed an increase in CD68<sup>+</sup> macrophage influx, mainly present in the outer two thirds of the scaffold, and with a predominant iNOS<sup>+</sup> M1 phenotype. A similar pattern was seen in the hep group at day 3.

In the IL-4/hep group, the CD68<sup>+</sup> macrophages were more homogeneously distributed throughout the scaffold, and stained

positive for both iNOS and Arg (Figure S4B, Supporting Information). At day 7, a large increase in CD68<sup>+</sup> macrophage presence was observed and they adopted a more elongated shape around the scaffold fibers in all experimental groups. There was a tendency to an increase in overall macrophage numbers in the IL-4/hep group, although there was a large variability between samples of the same group (Figure S5, Supporting Information). In the bare and hep groups, these macrophages adopted a predominant iNOS<sup>+</sup> M1 phenotype, whereas in the IL-4/hep group, the macrophages adopted a predominant Arg<sup>+</sup> M2 phenotype, suggesting the efficient induction of M2 polarization by IL-4 functionalization (Figure 2). At 3 months, the CD68<sup>+</sup> macrophages fused around the degrading scaffold remnants and were mainly positive for M1 marker iNOS in the bare and hep group, whereas in the IL-4/hep group, the fused CD68<sup>+</sup> macrophages were positive for both iNOS and Arg. The hep group showed the lowest amount of macrophages present (Figure S4C, Supporting Information).

#### 2.5. Cases of Local Hyperplasia in Heparin-Only Functionalized Grafts

After assessing the immunomodulatory effects of IL-4/hep functionalization in terms of macrophage polarization, we assessed the recruitment and phenotype of tissue cells. All experimental groups displayed local vWF<sup>+</sup> endothelial cells after 3 months of

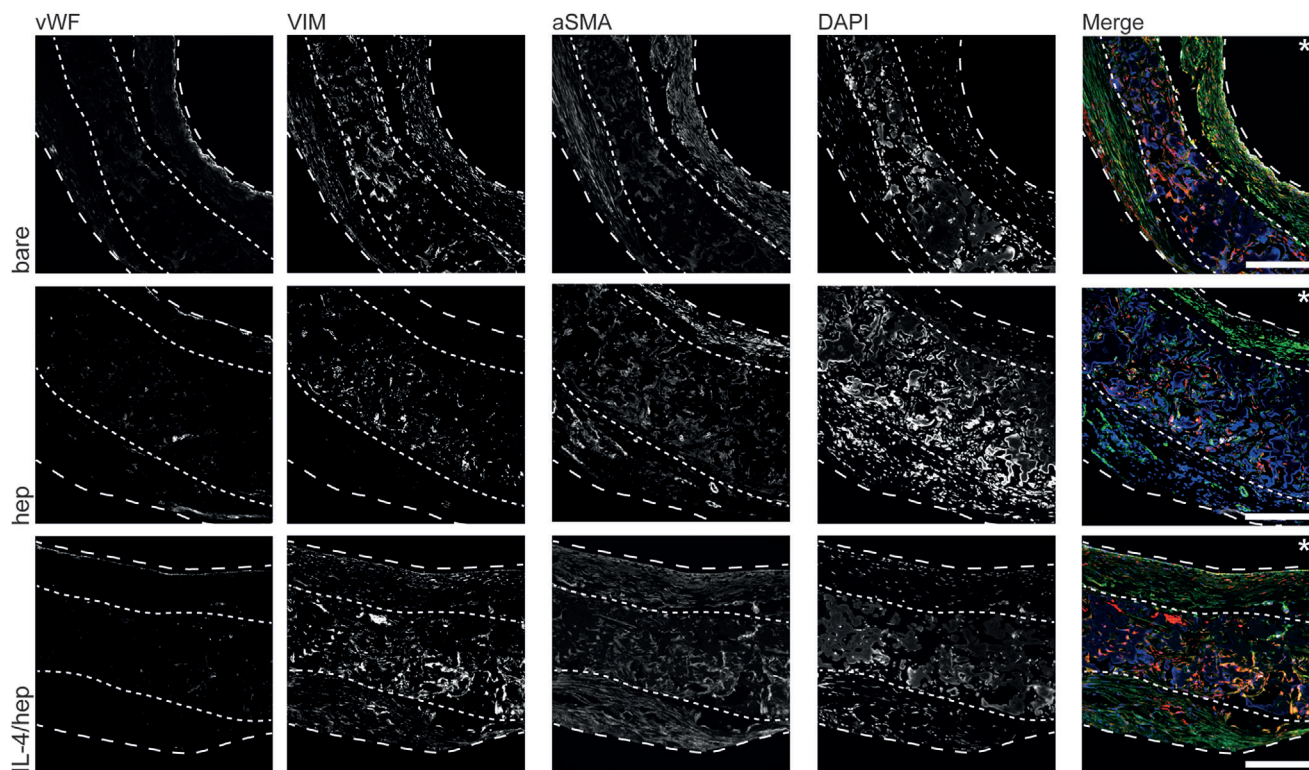


**Figure 3.** Cell phenotypes. Representative immunofluorescent staining of 3 month explants of all experimental groups (bare, hep, IL-4/hep) with vWF (white), VIM (red), aSMA (green) and cell nuclei (DAPI, blue) in grayscale and overlay. Abbreviations: von Willebrand Factor (vWF), vimentin (VIM), alpha smooth muscle actin (aSMA), heparin (hep), and interleukin (IL). \*Identifies the lumen. Scale bar: 200  $\mu$ m. Dashed lines indicate boundaries of the scaffold (densely dashed) and de novo tissue (loosely dashed).

implantation, which was most evident in the bare and IL-4/hep groups (Figure 3). At earlier timepoints, vWF<sup>+</sup> cells were not observed (data not shown). The presence of endothelial cells was confirmed by presence of CD31<sup>+</sup> endothelial cells on the graft luminal surface in all groups, as well as transmural ingrowth of small vessel structures through the degrading scaffolds (Figure S6, Supporting Information).

Within the degrading scaffold remnants, cells predominantly stained positive for the fibroblast marker vimentin. In addition, elongated  $\alpha$ SMA<sup>+</sup> cells with rod shaped nuclei were detected in the intimal tissue layer and on the adventitial side of the graft in the IL-4/hep and bare groups specifically. In the IL-4/hep group,  $\alpha$ SMA<sup>+</sup> cells were observed locally in between the degrading scaffold remnants. The hep group showed local intimal hyperplasia in some cases, with abundant deposition of  $\alpha$ SMA<sup>+</sup> cells at the luminal side (Figure 3) and hardly any  $\alpha$ SMA<sup>+</sup> cells at the adventitial side.

## 2.6. IL-4/Heparin Functionalization Influences Tissue Formation and Organization

DNA quantification revealed that all scaffolds were cellularized already at day 1 (Figure 4A). DNA amounts increased over time when comparing the early timepoints to the 3 month timepoint. Between the experimental groups, comparable DNA amounts

were found, although there was a relatively large variability between explants within each group, particularly at 3 months. Overall, DNA values for all experimental groups at all timepoints were higher than the DNA content of the native rat aorta. Sulphated glycosaminoglycan (GAG) quantification showed similar levels on day 1 and day 3 for all experimental groups, with a progressive increase in GAG content at day 7 and at 3 months. Some of the 3 month explants from the hep (3 out of 5) and the IL-4/hep (2 out of 5) group showed a GAG content comparable to the native aorta (Figure 4B). Hydroxyproline (HYP) and tropoelastin (ELN) were not detected at days 1, 3, and 7. At 3 months, HYP amounts did not significantly differ between the experimental groups, although HYP content tended to be lower content for the bare group explants. When compared to the HYP amounts of the native aorta, the HYP amounts were roughly 10 times lower in all experimental groups (Figure 4C). ELN contents were similar for all groups (Figure 4D).

In correspondence with the biochemical quantifications, Movat's pentachrome staining on 3 months explants showed neotissue formation in all experimental groups on both the adventitial and luminal sides of the grafts, as well as in between the degrading scaffold fibers (Figure S7, Supporting Information). Abundant collagen deposition and muscle-like tissue on the adventitial side was observed at 3 months for all the explants, although no strong fibrotic response was observed (Figure 4E; Figure S7, Supporting Information). Collagen deposition and GAG-rich ECM



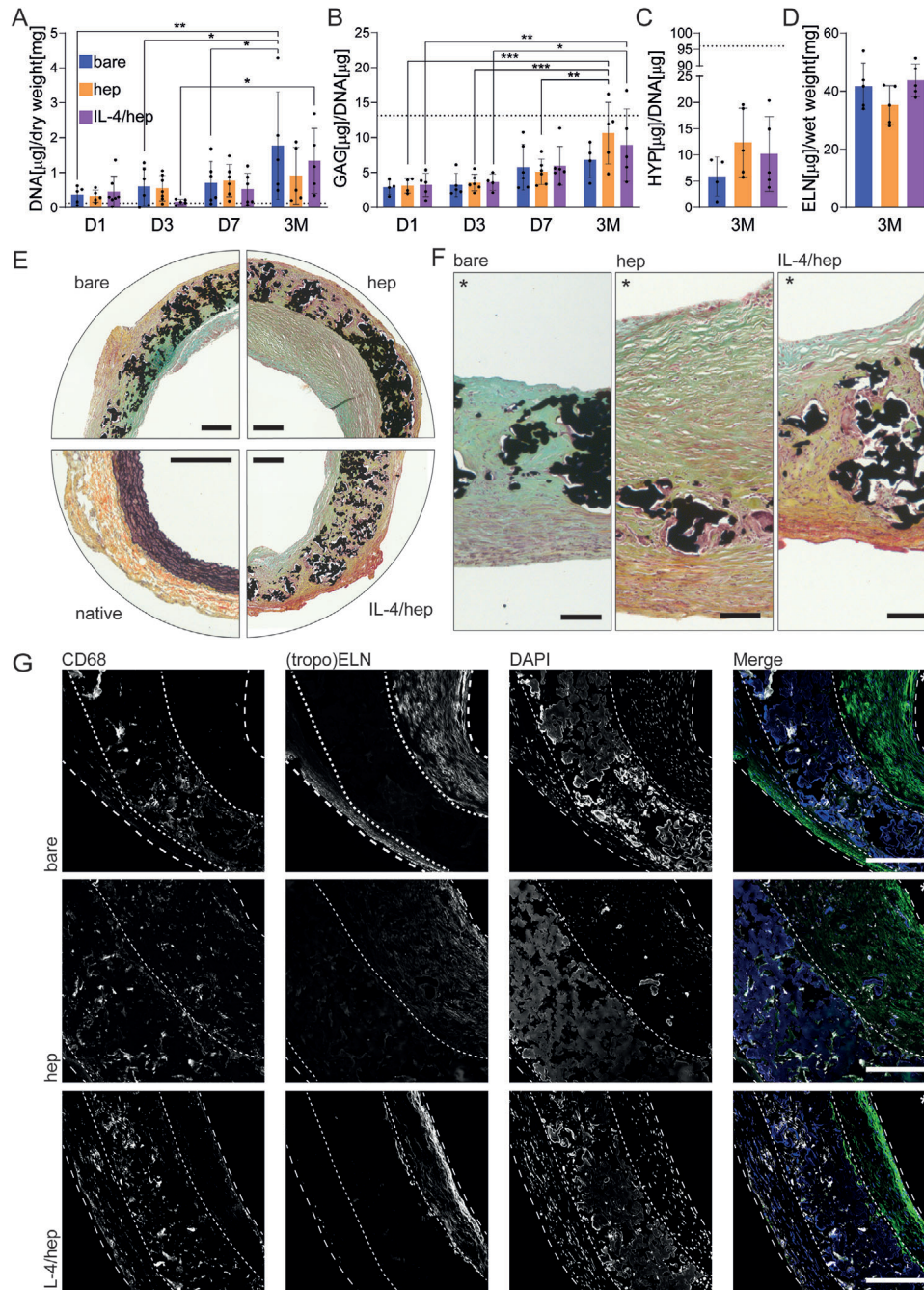


**Figure 4.** Tissue deposition and organization. A–D) Biochemical assays for quantification of DNA, GAG, HYP and ELN in explanted grafts of all experimental groups (bare, hep, IL-4/hep) and native rat aorta (dotted line). A) DNA content corrected against dry weight. B) GAG content corrected against DNA content. C) HYP content corrected against DNA content. D) ELN content corrected against wet weight. E–G) Representative images of 3 month explants of all experimental groups (bare, hep, IL-4/hep) and native rat aorta. E) Representative pentachrome staining depicting scaffold (black), collagen fibers and reticular fibers (yellow), ground substance (blue), fibrin (bright red), muscle (red). F) zoom of Pentachrome staining. G) Immunofluorescent staining of macrophage infiltration and elastin deposition with CD68<sup>+</sup> macrophages (red), (tropo) elastin (green), and cell nuclei (DAPI, blue) grayscale and merge zoom. \*Identifies the lumen. Dashed lines indicate boundaries of the scaffold (densely dashed) and tissue (loosely dashed). Data for biochemical assays presented as mean  $\pm$  SD,  $n = 5$ –7 per group (for absolute numbers analyzed per group per timepoint see Table 1).  $p$ -values for DNA and GAG assays are calculated using two-way ANOVA following Tukey post hoc test.  $p$ -values for HYP and ELN were calculated using the non-parametric Kruskal–Wallis test with a Dunn’s multiple comparison test. Significant differences are presented as \* $p < 0.05$ , \*\* $p < 0.01$ , and \*\*\* $p < 0.001$ . Abbreviations: sulphated glycosaminoglycan (GAG), hydroxyproline (HYP), tropoelastin (ELN), heparin (hep), and interleukin (IL). Scale bar in tile scans and immunofluorescent images: 200  $\mu\text{m}$  (E,G), in pentachrome zooms: 100  $\mu\text{m}$  (F).

were observed in between the degrading fibers in all groups, but was most clear in the IL-4/hep and bare group. Close-up images of the pentachrome staining indicated local “bridging” structures of tissue at locations where the graft fibers were resorbed. This was mainly observed in the IL-4/hep and bare group, as these groups tended to show more signs of scaffold resorption (Figure 4F). In some of the grafts (1/5 of the bare grafts, 2/5 of the hep graft and 2/5 IL-4/hep grafts), first signs of potential developing calcifications, manifested as cartilage-like GAG accumulations, were detected around the degrading scaffold fibers, regardless of functionalization or location (Figure 4E, dark green areas).

## 2.7. IL-4/Heparin Functionalization Improves Immature (Tropo)Elastin Organization

To assess the deposition and organization of elastin, an immunofluorescent antibody staining for (tropo)elastin was performed, in costaining with the pan-macrophage marker CD68. The stainings revealed a strong deposition of (tropo)elastin, particularly in the luminal layer of neotissue in all grafts (Figure 4G), which corresponds to the biochemical quantification (Figure 4D). (Tropo)elastin expression did not colocalize with the macrophages. Although (tropo)elastin was detected in all groups, there was a much more aligned, subendothelial localized (tropo)elastin deposition in the IL-4/hep group when compared to the hep and bare groups. In the hep group in particular, the (tropo)elastin was deposited in a more chaotic way (Figure 4G).

## 2.8. IL-4-Heparin Functionalized Grafts Showed More Mature ECM

To assess the composition and maturity of the regenerated tissue, Raman microspectroscopy was used to detect the local molecular composition in the various groups, which was compared to the composition of native arterial tissue using true component analysis (TCA). TCA was used for the identification of components describing the distributions of synthetic material, collagen and actin-rich regions across the spectral map. Subsequently, spectral differences between functionalization groups or between the explants and native artery were evaluated using principal component analysis (PCA).

Raman imaging and TCA identified and localized the representative native arterial wall ECM components in the explanted grafts (Figure 5A). The multilayered native arterial wall comprised a collagen-rich adventitial layer, defined elastic fibers and an actin-rich intima. The spectral features of the identified TCA components (Figure S8, Supporting Information) match the biological fingerprint of collagen, elastin and actin.<sup>[31–34]</sup> De novo ECM formation in the grafts was characterized in the breakdown of the scaffold material after 3 months and its envelopment by a thick layer of ECM, primary composed by a mixture of collagen and actin-rich proteins (Figure 5A). No spectral component could be identified for mature elastin in any of the TCAs of the explanted samples, which is in correspondence to the absence of the typical black mature elastin fibers in Movat's pentachrome staining (Figure 4E,F).

The composition of the newly formed tissue in explanted grafts was further compared to the native arterial ECM by PCA. To that

end, first, the native arterial ECM was further assessed by PCA to serve as reference for the de novo regenerated ECM in the grafts (Figure 5B,C). Native elastin spectral features were described by negative scores for both principal component (PC) 1 and PC 3. PC 1 and PC 2 were both positive for native collagen and, finally, native intima clustered at negative PC 2 score ranges and positive PC 1 and PC 3 ranges. Based on the PC loadings (Figure 5D), PC 1 exhibited representative Raman bands for native collagen at 1064, 1134, 1248, 1275, and 1392  $\text{cm}^{-1}$ . Native elastin spectral features were mostly described by negative PC 3 loadings including peaks at 908, 1108, and 1340  $\text{cm}^{-1}$ .<sup>[31]</sup> Spectral differences in the native intima are indicated by negative bands in PC 2 and positive bands in PC 3 loadings, dominated by the two bands at 1134 and 1297  $\text{cm}^{-1}$ . Furthermore, the broad amide I band located around 1660  $\text{cm}^{-1}$  showed high variation between the three native ECM proteins (Figure S8, Supporting Information). Amide I band topography gives insight into the secondary structure of complex proteins, depending on the contribution of the structural Raman peaks at 1635 and 1670  $\text{cm}^{-1}$  to the profile of the amide I band.<sup>[35]</sup>

PCA projection of the explant spectral datasets (collagen and actin) into the native ECM PCA model allowed to independently compare native ECM to the de novo ECM in the grafts (Figure 5E–G). Comparison of average score values revealed similar trends of the projected de novo ECM data to their native ECM structure equivalents. In averaged PC 1 scores (Figure 5E), both native collagen and de novo collagen spectra from all graft types closely clustered together at positive score values. PC 2 separated native intima at negative score values from native collagen and elastin (Figure 5F). Actin-rich neotissue was projected to the same scores ranges as native intima tissue. Finally, negative PC 3 scores were assigned to native elastin samples whereas none of the de novo ECM spectra cluster in the same range (Figure 5G). The PCA projection further confirms the presence of mature collagen and actin rich intima-related proteins in the explanted grafts in general, as well as the absence of mature elastin as indicated in the TCA images and histological analysis.

The effect of scaffold functionalization on de novo ECM synthesis was investigated by PCA (Figure 6). De novo collagen data originating from bare and hep scaffolds mostly overlapped and locate at positive range of PC 2 (Figure 6A), whereas IL-4/hep exhibited negative scores for PC 2, even though a high degree of heterogeneity within the animals was observed (Figure 6C). For PCA comparison of the actin signatures, similarly to de novo collagen, the explanted actin-rich tissue from bare and hep functionalized scaffolds overlapped in the positive range of PC 2 (Figure 6B). The cluster for the IL-4/hep group can be found on the negative side of PC 2. However, also this dataset showed a very heterogeneous distribution (Figure 6D). The PC loadings for de novo collagen and actin-rich components (Figure 6E) exhibited positive Raman bands at 858, 940, and 1043  $\text{cm}^{-1}$  assigned to proline, and 1008  $\text{cm}^{-1}$ , which is linked to phenylalanine. Additional bands at 1250 and 1272  $\text{cm}^{-1}$  for amide III and 1670  $\text{cm}^{-1}$  for amide I, indicate a higher protein content in the bare and hep de novo ECMs. The most prominent negative peak at 1585  $\text{cm}^{-1}$  is associated to hydroxyproline and is more prevalent in the IL-4/hep group ECMs.

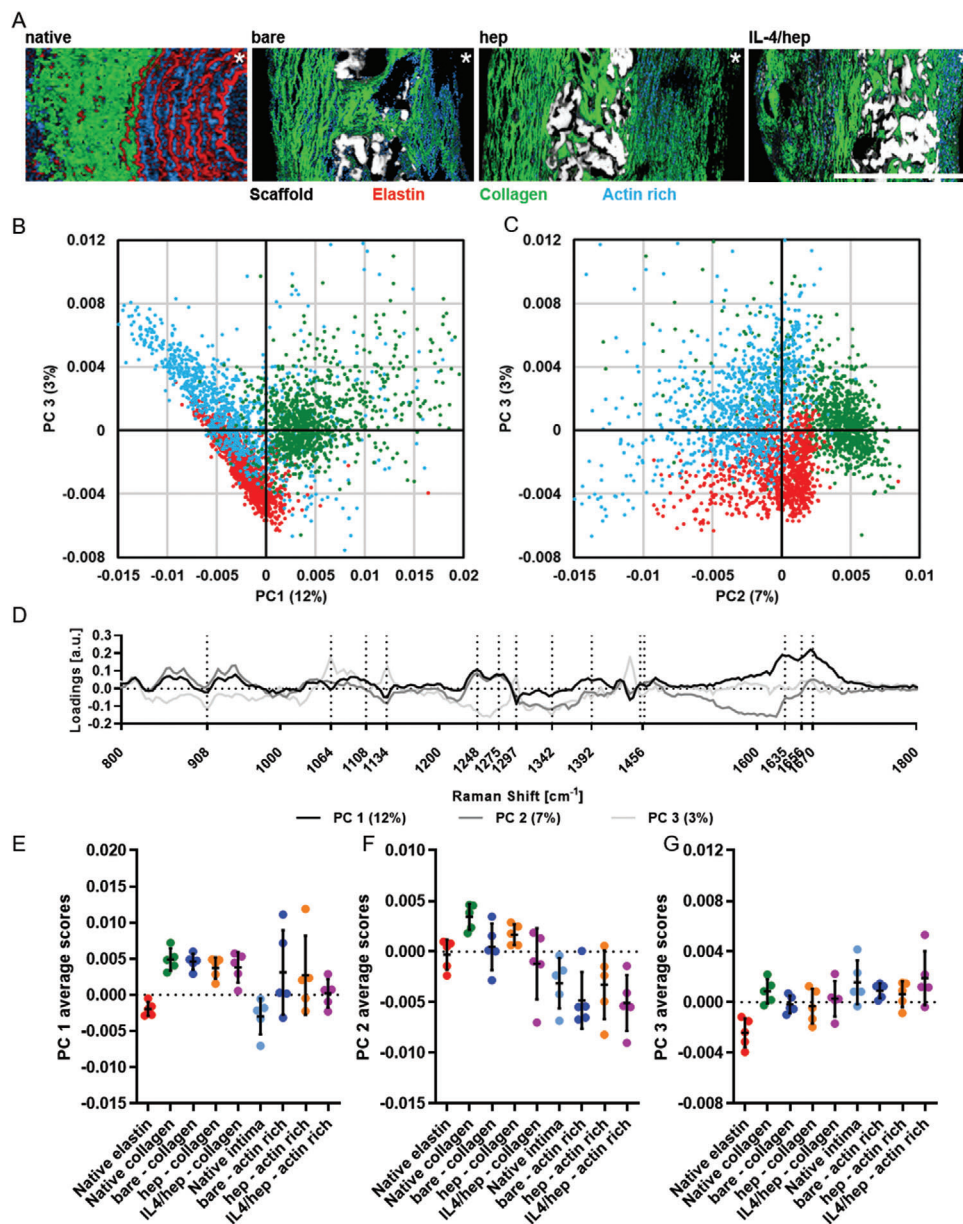


**Figure 5.** ECM remodeling based on Raman spectra TCA of 3 months vascular graft explants of all experimental groups (bare, hep, IL-4/hep). A) Representative Raman images depicting the distributions for elastin (red), collagen (green) actin rich (blue) and scaffold (white) components of native aorta as well as bare, hep and IL-4/hep functionalized grafts. Scale bar: 300  $\mu\text{m}$ , \*Identifies the lumen. Score plots for B) PC 1 versus PC 3 and C) PC 2 versus PC3 and D) corresponding loadings for native ECM components PCA. Average PC scores of E) PC 1, F) PC 2 and G) PC 3 for PCA projection of de novo ECM from bare (dark blue), hep (orange) and IL-4/hep (purple) into native ECM PCA. Data for average PC scores are presented as mean  $\pm$  SD,  $n = 5$  per experimental group.  $p$ -values were calculated using one-way ANOVA with Tukey correction. Abbreviations: True component analysis (TCA), principal component analysis (PCA), principal component (PC), heparin (hep), IL (interleukin), and extracellular matrix (ECM).

### 2.9. Minor Variations in Scaffold Resorption between Experimental Groups

To achieve tissue homeostasis, a delicate balance between tissue production and biomaterial resorption is required. Both Raman spectroscopy as well as SEM analysis were used to assess the extent of resorption of the synthetic graft material. After 3 months of implantation, PCA revealed differences between the implanted graft material and the material pre-implantation (Figure 7A).

Analysis of average score values showed minor differences between the differently functionalized materials. PC1 indicated a separation of the bare and hep groups, whereas IL-4/hep clustered closer to the material pre-implantation (Figure 7B). However, the loadings plot signature mainly referred to a difference based on the amount of infiltrating ECM tissue according to an increasing amide I band as the only relevant spectral feature (Figure 7C). A resorption-dependent signature was featured by PC 2, where major chemical alterations were assigned to a

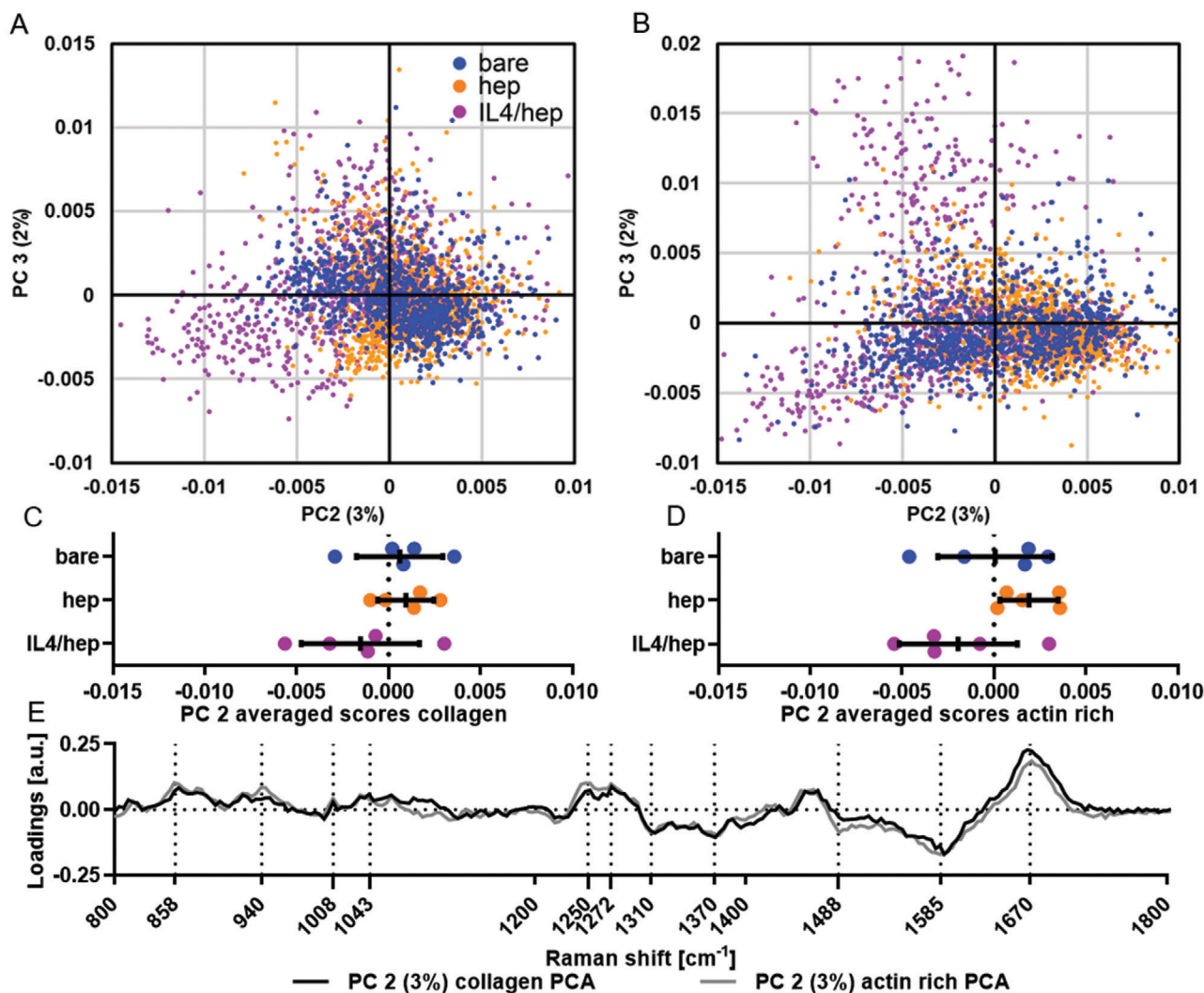


**Figure 6.** PCAs for de novo ECM of bare (dark blue), hep (orange) and IL-4/hep (purple) groups. PC 2 versus PC 3 scores plots for A) collagen and B) actin rich components. PC 2 averaged scores for C) collagen and D) actin rich. E) PC 2 loadings. Data for average PC scores are presented as mean  $\pm$  SD,  $n = 5$  per experimental group.  $p$ -values are calculated using one-way ANOVA with Tukey correction. Abbreviations: true component analysis (TCA), principal component analysis (PCA), principal component (PC), heparin (hep), and IL (interleukin).

decrease in the 1436 and 1720  $\text{cm}^{-1}$  polymer bands, which correspond to the  $\text{CH}_2$  bend and the carbonyl ( $\text{C}=\text{O}$ ) stretch of the PCL block in the polymer, respectively.<sup>[36]</sup> Resorption on the molecular level in IL-4/hep functionalized scaffolds was highly heterogeneous.

To qualitatively assess the graft resorption, explants were decellularized and fiber morphology was visualized with SEM. The weight of the removed cells and tissue versus the remaining scaffold weights were similar for all experimental groups at the early timepoints time points, which is similar to the observations of the biochemical assays of the early timepoints (Figure 4A–D). The ratio between cells + tissue and remaining scaffold became larger after 3 months for all experimental groups, indicating replacement of scaffold material with endogenously formed tissue at 3 months (Figure 7D). When comparing the explants of day 1 to a non-implanted graft (Figure 7E, left), it could be observed that right upon implantation of the graft, drastic fiber expansion oc-

curred. This fiber expansion seemed to result in fiber fusion, especially on the luminal side of the graft, starting already at day 1 for the hep and the bare group and from day 3 in all experimental groups (Figure S9, Supporting Information). The swelling of the fibers seems to correlate with the increase in graft wall thickness (Figure S2G, Supporting Information) and slightly lower lumen diameter (Figure S2H, Supporting Information) directly after implantation when compared to the preimplanted graft (Figure S2E, Supporting Information).

Some first signs of fiber cleavage, indicative of oxidative resorption,<sup>[37]</sup> appeared already at day 7 (Figure 7E, middle) in all groups, but was mainly observed in the IL-4/hep group on the outer side of the graft (Figure S9, Supporting Information). At 3 months, all experimental groups showed fiber cleavage (Figure 7E, right). In addition, the extent of scaffold degradation was indirectly assessed via GPC for 2 samples per group per timepoint (Figure S10, Supporting Information). These

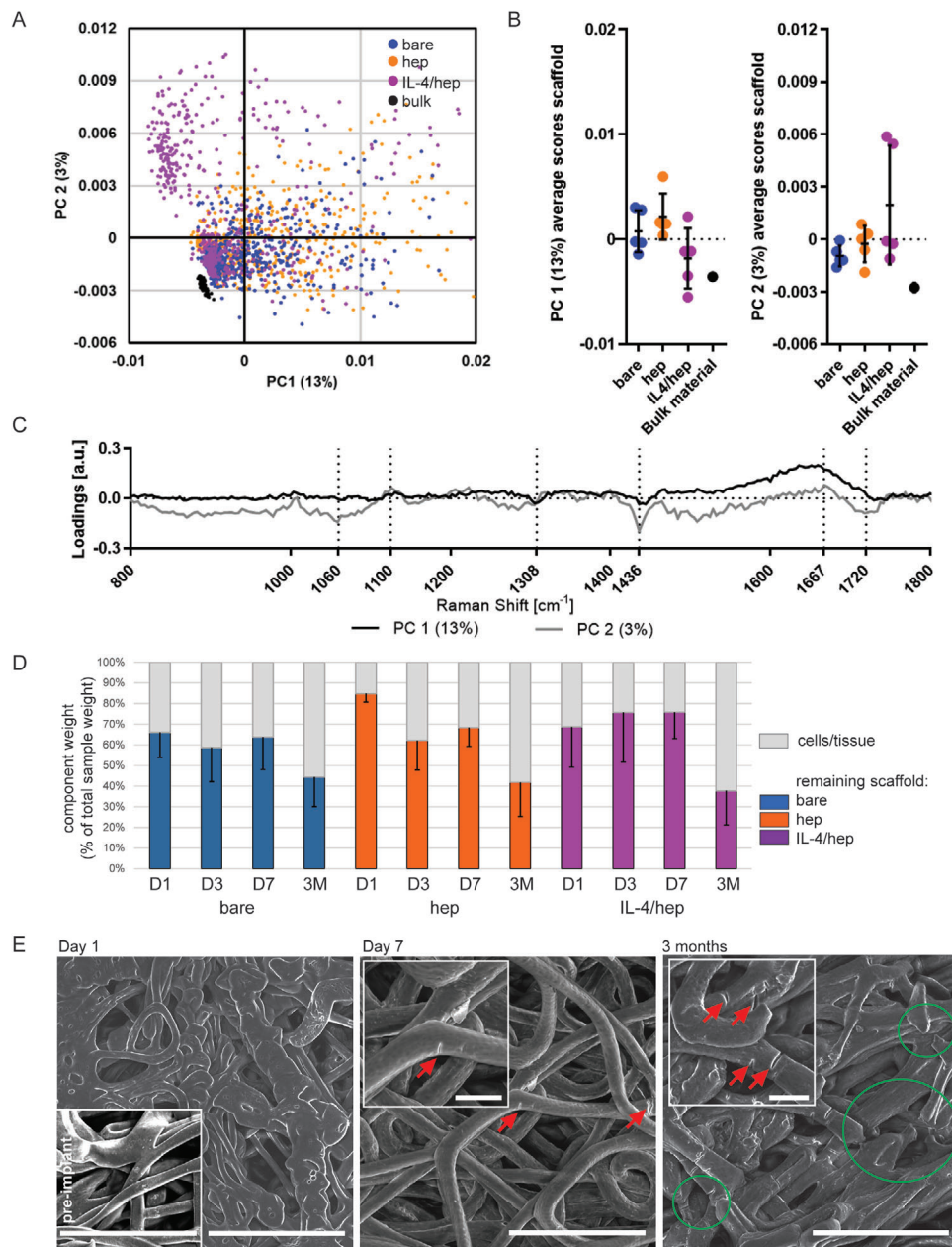


**Figure 7.** Scaffold resorption. A) PC 1 versus PC 2 score plots for scaffold material PCA at 3 months. B) Average PC 1 (right) and PC 2 (left) scores selected by material TCA mask for bare (dark blue), hep (orange), IL-4/hep (purple) and bulk material (black). C) Loadings for PC1 and PC2. D) Component weight (% of total sample weight) of removed cells + tissue and remaining scaffold during decellularization procedure for SEM imaging. E) SEM images of decellularized scaffolds, representative for all experimental groups, showing swelling of fibers already after 1 day of implantation (see comparison with pre-implant in insert), first signs of fiber cleavage after 7 days, and fiber breakage after 3 months. See Figure S9 (Supporting Information) for SEM images of decellularized scaffold from luminal and adventitial side for all experimental groups at all timepoints. Data for average PC scores are presented as mean  $\pm$  SD,  $n = 5$  per experimental group and  $n = 1$  for bulk material.  $p$ -values are calculated using one-way ANOVA with Tukey correction. Data for component weight are presented as mean  $\pm$  SD,  $n = 5-7$  (for absolute numbers analyzed per group per timepoint see Table 1). Abbreviations: principal component (PC), principal component analysis (PCA), heparin (hep), and interleukin (IL). Red arrows indicate fiber cleavage, green circles indicate fiber breakage. Scale bars 100  $\mu$ m (large SEM images and insert pre-implant), inserts with zooms day 7 and 3 months: 20  $\mu$ m.

preliminary results indicated that regardless of the experimental group, both  $M_n$  and  $M_w$  were comparable for day 1, day 3, and day 7, but reduced at 3 months, indicative of resorption. No significant differences were observed between the different functionalized groups.

## 2.10. Mechanical Characterization

Uniaxial tensile tests on rings of explanted grafts showed a change in mechanical behavior between the early (day 1, day 3, and day 7), and late timepoints (3 months; **Figure 8**). At day 1 and

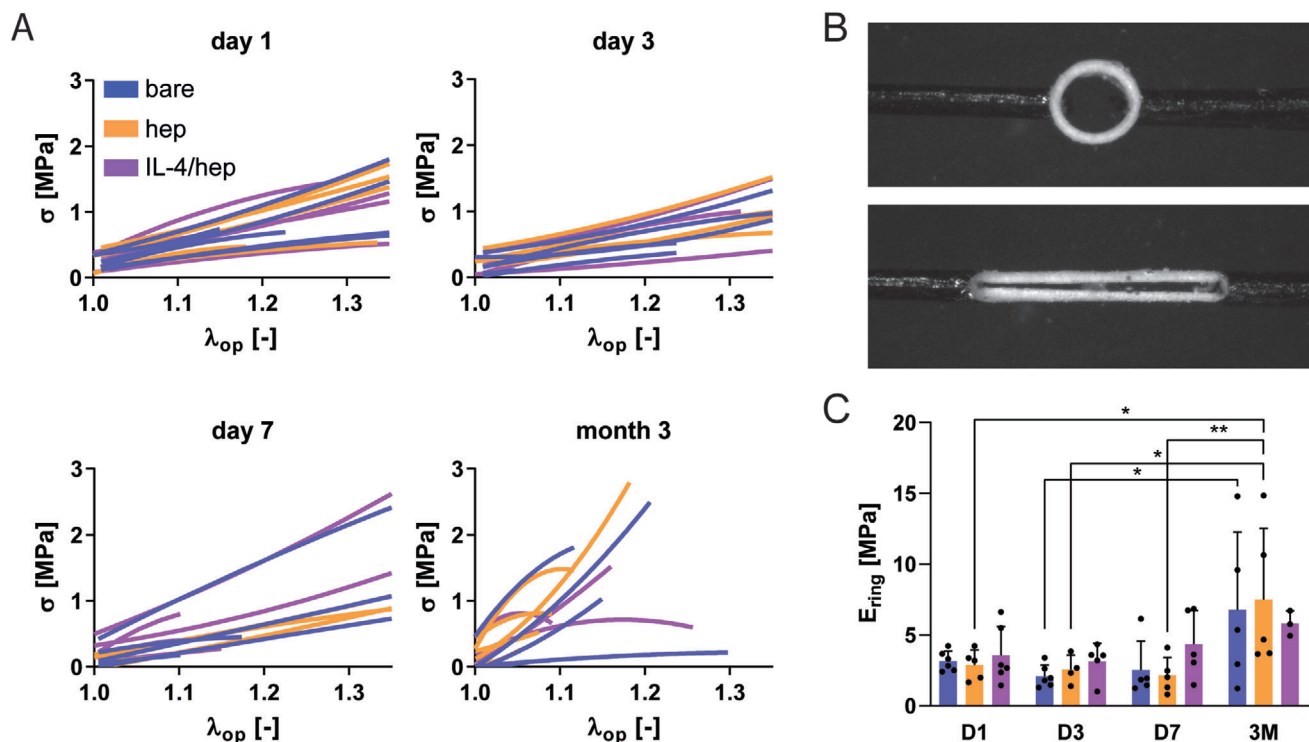


**Figure 8.** Uniaxial ring tests of aortic grafts. A) Stress–stretch curves of explanted grafts for all experimental groups (bare, hep, IL-4/hep). B) Representative image of sample subjected to uniaxial ring test. C) Temporal changes in  $E_{ring}$  during implantation time. Data for  $E_{ring}$  are presented as mean  $\pm$  SD,  $n = 5$ –7 (for absolute numbers analyzed per group per timepoint see Table 1).  $p$ -values are calculated using two-way ANOVA following Tukey post hoc test. Abbreviations: heparin (hep), interleukin (IL), stress ( $\sigma$ ), stretch outer perimeter ( $\lambda_{op}$ ), and Young’s modulus ( $E$ ). Significant differences are presented as \* $p < 0.05$ , \*\* $p < 0.01$ , and \*\*\* $p < 0.001$ .

day 3, all explants from all experimental groups showed similar stress-strain stress curves. At day 7, the explants of the hep group tended to have a slightly lower stiffness when compared to the explants from the IL-4/hep group (not significant). At 3 months, explants from the bare and hep group increased significantly in stiffness, compared to the explants from the early timepoints. At this timepoint, the hep group tended to have a higher stiffness than the IL-4/hep group (Figure 8C).

### 3. Discussion

This study evaluated the potential of vascular grafts made from a novel supramolecular material that allows for simple post-processing functionalization with heparin and IL-4.<sup>[23]</sup> Grafts remained functional up to 3 months without thrombosis, aneurysm or rupture at the anastomoses. We demonstrated that functionalization with IL-4/hep influenced macrophage recruitment and polarization, led to improved immature (tropo)elastin deposition, and allowed for more mature ECM formation. Notably, heterogeneity within the experimental groups was observed over the full range of analyses, which warrants attention for future clinical translation.

The use of supramolecular chemistry as applied here offers several important advantages for the tailored engineering of scaffolds for in situ tissue engineering applications. The supramolecular building blocks with matching supramolecular motifs form a material with tailorable properties. This en-

ables both the introduction of functional motifs and bioactive components and allows for tunable mechanical and degradative properties.<sup>[38]</sup> The feasibility of these supramolecular graft materials is shown by several in vivo studies for various applications, ranging from meshes for abdominal wall reconstruction<sup>[39]</sup> to vascular grafts<sup>[40,41]</sup> and heart valves.<sup>[42–44]</sup> By immobilizing heparin using a supramolecular incorporated heparin-binding peptide as described in this study, the protein binding properties of heparin can be modularly exploited to bind additional growth factors or cytokines. One major advantage of this sequential approach is that the functionalization with both heparin and IL-4 is done after processing the material into 3D vascular grafts, thereby preventing potential damage to the proteins during the electrospinning process. We previously validated the effectiveness of this approach in vitro to create stable functionalized grafts, verifying the functional IL-4/heparin immobilization was demonstrated over time, not only in static conditions, but also under physiological flow.<sup>[23]</sup> Based on these in vitro results, we designed the current in vivo study, in which the IL-4/heparin functionalized material was assessed for its use as a regenerative vascular graft.

Heparin functionalization of synthetic small-diameter TEVGs is an often-reported strategy to prevent thrombus formation.<sup>[45–54]</sup> Surprisingly, we did not observe a clear reduction in platelet activation in the hep group when compared to bare group (Figure S3, Supporting Information). This

observation, in case of heparin functionalized groups (either with or without IL-4), is in apparent contrast with the canonical definition of heparin as a potent anticoagulant. The inhibitory action of heparin on fibrin formation is based on its ability to bind antithrombin III (AT-III) and its inhibitory action on thrombin.<sup>[55]</sup> While the heparin sodium salt used in this study has a molecular weight in the range of 17 000–19 000 Da, which should ensure accommodation of both AT-III and thrombin, we speculate that accessibility and availability of the heparin's negatively charged groups for AT-III activation purposed might be limited by the electrostatic interactions occurring between the heparin and the UPy-HBP. Nevertheless, thrombus formation was not a significant reason for graft failure in any of the graft types in this study, which might be attributed to the relatively oversized luminal diameter of the vascular grafts (2000  $\mu\text{m}$ ) when compared to the native rat aorta (1100  $\mu\text{m}$ ) (Figure S2H, Supporting Information).

An interesting observation in this study is the occurrence of cases of hyperplasia and less mature tissue formation the heparin-only group, while the neointima formation in the IL-4/hep and bare groups remained limited. This is in line with the increased presence of the observed  $\alpha\text{SMA}^+$  rich neointimal layer in the heparin-only group. The effect of heparin on hyperplasia remains controversial. With the development of methods for covalent conjugation using end-point immobilization, heparin has been conjugated to commercialized vascular grafts, such as ePTFE grafts. However, in both sheep<sup>[56]</sup> and rat models,<sup>[45]</sup> heparin immobilization did not prevent intimal hyperplasia. The latter was also confirmed in vitro, in a study that showed that rat aortic smooth muscle cells became resistant to the antiproliferative activity of heparin following long term heparin treatment.<sup>[57]</sup> Concurrently, heparin conjugation has led to inconsistent results on vascular patency and tissue remodeling in in situ TEVGs. Several studies showed a positive effect of heparin functionalization of small-diameter TEVGs on patency and tissue regeneration.<sup>[45–49,58,59]</sup> A recent example is a study by Matsuzaki et al., in which higher patency rates (85%) were reported for heparin-eluting bilayered polycaprolactone/poly(L-lactide-co-caprolactone) (PCL-PLCL) vascular grafts compared to non-heparin grafts (20%) in carotid artery interposition replacement during 8 weeks follow-up in sheep.<sup>[50]</sup> In contrast, other studies report adverse events with the heparin functionalization of small-diameter TEVGs, with local formation of an  $\alpha\text{SMA}$ -rich neointimal layer in heparin functionalized grafts.<sup>[51,52,60]</sup> One example is the study by Jiang et al., in which excessive neointimal hyperplasia was reported in heparinized grafts made from vascular ECM in rats.<sup>[52]</sup> Another example is the study of Koobatian et al., who showed rapid occlusion of heparin-functionalized cell-free small intestine submucosa (SIS) within 2 days after carotid artery implantation in sheep.<sup>[53]</sup>

The cause for local hyperplasia formation in multiple explants of the heparin-only group in our study, as well as others, remains unclear. We speculate that this may be caused by the local sequestering of mitogenic and fibrogenic growth factors, as heparin has a high binding affinity for many growth factors in the circulating blood (e.g., VEGF).<sup>[46]</sup> In a recent study, Feng et al. characterized the endogenous growth factors (platelet-derived growth factor, PDGF; basic fibroblast growth factor, bFGF; VEGF) that bound to a subcutaneously injectable heparin polysaccharide hy-

drogel in mice.<sup>[61]</sup> Moreover, when exposed to macrophages, they showed that heparin locally sequesters the macrophage produced growth factors. While potential effects of heparin by itself on macrophage polarization have been suggested,<sup>[62]</sup> no clear effect of heparin on macrophage polarization was observed as the bare and heparin group both showed a trend toward more M1 (iNOS+) macrophages and lower M2 (Arg+) macrophages, which is in correspondence to our previous in vitro data on this materials.<sup>[23]</sup> This may explain why we did not observe hyperplasia in the IL-4/hep dual-functionalized group, as the growth factor and cytokine release profile would be altered by the IL-4-induced macrophage polarization, although this warrants further investigation.

One of the main findings of this study is that early modulation of macrophage phenotype led to more mature tissue formation 3 months downstream. IL-4 functionalization promoted the presence of M2 macrophages in vivo, particularly within the first week of implantation. This led to differences in the downstream tissue maturation and organization. These findings are in line with previous reports in which IL-4 functionalization is employed to direct macrophage polarization for vascular tissue regeneration.<sup>[63,64]</sup> To explain this, it is essential to consider the kinetics of the various material functionalizations and the resulting kinetics of the in vivo response. Although we were unable to reliably quantify for how long the initially incorporated IL-4 was retained and active in vivo, we previously established persistent retention of approximately 80% of the IL-4 up to 7 days under physiologic flow conditions in vitro.<sup>[23]</sup> The observed dominance of M2 polarization at 7 days in vivo in the IL-4 group strongly suggests that the IL-4 is still present and active at this time point in vivo as well. Considering the typical host response to a synthetic implant, acutely after implantation, the synthetic material will instantaneously be covered in proteins and signaling factors, including blood proteins and DAMPs released due to the induced tissue damage that initially recruit neutrophils predominantly. The macrophages are subsequently attracted by cytokines released from the neutrophils that are unable to phagocytose the material. We did not observe any significant differences in neutrophil recruitment to the differently functionalized grafts, nor in overall cell influx numbers. In addition, from the current data it is clear that the effect of the IL-4 on the macrophages is most pronounced at day 7. From those observations we can conclude that 1) the initial protein coverage did not prevent the bioactivity of the IL-4 and 2) that the effect of the IL-4 is predominantly on steering the phenotype of inflammation-recruited macrophages. Interestingly, we did observe a tendency toward an increased macrophage influx in the IL-4 group at 7 days, in addition to enhanced M2 polarization. This may point to an effect of IL-4 on the monocyte-recruiting ability of early inflammatory cells, such as neutrophils or mast cells, or to a direct chemotactic effect of IL-4 on macrophage recruitment, although these signaling mechanisms are complex and dynamic and there is conflicting evidence in literature in that respect. Since it is known that early macrophage phenotype is predictive for downstream tissue formation, we hypothesize that the early induction of an IL-4-primed M2 macrophage phenotype is directly responsible for the more mature tissue formation at 3 months. We speculate that the observed beneficial effects at 3 months follow-up were at least partly downstream effects of the early shift to an M2/T<sub>H</sub>2 dominated

inflammatory environment, propagated by cell-produced anti-inflammatory cytokine signaling, rather than a direct effect of the initially incorporated IL-4. The detection of T<sub>H</sub>2 cells, which were previously shown to be required to form an IL-4-mediated pro-regenerative biomaterial scaffold microenvironment,<sup>[24]</sup> was inconclusive in the present study. In this study we opted to focus on Raman microspectroscopy to gain temporal information on the scaffold and ECM formation over time. For follow-up studies, it would be valuable to characterize the sequestered proteins on the explants over time, by using for example a proteomics approach as performed by Swartzlander et al. on subcutaneous hydrogel implants,<sup>[65]</sup> and to unravel the resulting temporal course of immunological and other cellular events using dedicated study designs.

The detailed evaluation of the matrix maturation and organization using Raman microspectroscopy revealed important differences in tissue maturation between the functionalization groups that could not be detected by purely quantifying gross ECM production as determined via biochemical assays. Specifically, Raman microspectroscopy suggested that bare and heparin-functionalized scaffolds induced condensed protein structures in the de novo synthesized ECM. Meanwhile, IL-4/hep functionalization allowed for the formation of a more stable ECM by promoting the deposition of hydroxyproline. This is evident from the PCA scores, which indicated a high hydroxyproline content for the IL-4/hep group, which has been reported in correlation to more stable collagen triple helices.<sup>[66]</sup> Moreover, although (tropo)elastin was detected in all groups, there was a much more aligned, subendothelial localized (tropo)elastin structure in the IL-4/hep group when compared to the hep and bare groups, which displayed (tropo)elastin deposition in a less aligned and more chaotic fashion. Despite that the deposition of well-organized (tropo)elastin in the IL-4/hep group is encouraging, this did not yet translate into the formation of mature elastic fibers at the timepoints studied. As can be observed in the pentachrome staining, the typical black mature elastin fibers seen in native rat aorta were not visible in the explants. Similarly, the Raman analysis showed the absence of mature elastin in all 3 months explants. It is most likely that the (tropo)elastin visualized in immunofluorescent staining and measured in the biochemical assay, are still immature (tropo)elastin fibers, which are not detectable by the pentachrome staining. Although no mature elastin fibers were formed within the 3 months follow-up time of this study, the observation of more aligned (tropo)elastin in the luminal layer of the IL-4/hep grafts is encouraging and suggests potential for mature elastic network regeneration in situ. Interestingly, the (tropo)elastin deposition did not colocalize with macrophage presence. This is in line with recent findings by Duijvelshoff et al., who demonstrated a progressive regeneration of mature elastic fibers accompanied by a progressive decrease in macrophage presence in regenerative resorbable synthetic stents.<sup>[67]</sup> It is plausible that the early pro-regenerative environment induced by IL-4 contributes to a more favorable biochemical milieu for elastin accumulation, for example by limiting the secretion of elastase by pro-inflammatory macrophages.<sup>[68]</sup>

In terms of scaffold resorption, no clear differences were detected between the functionalization groups. Pit formation and cavitation, indicative of (macrophage-driven) enzymatically accel-

erated hydrolysis,<sup>[37,69,70]</sup> mainly occurred at the adventitial side of the graft, although it was also visible on the luminal side. The bare and the IL-4/hep group showed the clearest pit formation on the adventitial side of the graft at the early timepoints, which is in accordance with the observation that the CD68<sup>+</sup> macrophages were mainly present in the outer two-thirds of the graft. Over time, all grafts progressively resorbed through a combination of enzymatically accelerated hydrolysis and oxidative resorption, as also previously reported.<sup>[37]</sup> This was also reflected in the mechanical properties of the explants, which displayed a shift from scaffold-dominated mechanical properties at the early timepoints to a more stiff, collagen-dominated behavior after 3 months, as also previously observed for in situ tissue-engineered heart valves.<sup>[43,71]</sup> How the mechanical properties will change over longer time-periods, when more scaffold is resorbed, remains to be elucidated with longer follow-up. Nevertheless, we conclude that for all groups the mechanical stability was stable enough over time to allow for vascular function as no rupture or aneurysm occurred. Notably, substantial variability in graft mechanical properties was detected between grafts within each group, which was most pronounced at 3 months. Variability in homogenous experimental groups for in situ TEVGs has been acknowledged and reported by our group previously in a recent study using supramolecular elastomeric TEVGs in rats by Duijvelshoff et al.,<sup>[14]</sup> as well as by other groups.<sup>[72,73]</sup> For example, Khosravi et al. showed variability in graft, stiffness of polyglycolic acid-poly( $\epsilon$ -caprolactone/lactic acid)-based scaffolds in mice,<sup>[72]</sup> and Bergmeister et al. showed variable resorption profiles in a study with thermoplastic polyurethane (TPU) vascular grafts in rats.<sup>[73]</sup> These variabilities might have derived from differences in the remodeling potential of the individual animals and are an important point of attention toward robust clinical application for in situ TEVGs.

Importantly, in this study, the anastomotic sides of the vascular graft were shielded with impenetrable GoreTex strips to prevent rapid anastomotic ingrowth, using a previously established model.<sup>[18]</sup> It is known that trans-anastomotic cell infiltration and endothelialization is restricted to the immediate perianastomotic region only in humans,<sup>[74,75]</sup> which is in contrast to rodents, in which trans-anastomotic ingrowth of mature endothelial and smooth muscle cells is the predominant mechanism of graft infiltration and the cause of tissue deposition.<sup>[17]</sup> It should be noted that the GoreTex shields were slightly tapered in order to bridge the size mismatch between the grafts and the native aorta and ensure smooth blood flow over the anastomotic regions. An observed lack of colocalization of  $\alpha$ SMA and vWF in our stainings suggests that endothelial-to-mesenchymal-transition (endoMT) was limited to absent. The impeded transanastomotic cell infiltration due to the use of the impenetrable GoreTex shielding, and the apparent absence of endoMT, suggests that infiltrating blood-derived  $\alpha$ SMA<sup>+</sup> cells descend at least partially from transmural ingrowth, as previously reported.<sup>[76]</sup> Transmural ingrowth of small capillary and vessel-like structures on the adventitial side and through the porous graft was confirmed with a CD31 immunofluorescent staining (Figure S6C, Supporting Information), indicating that the pore size and resorption rate of the graft material was adequate to allow for transmural ingrowth.<sup>[77]</sup> The enabling of transmural ingrowth also promoted the absence of



a severe fibrous encapsulation as a result of the foreign body response, as it is well-established that sufficient pore size is an important modulator of fibrous encapsulation and promotor of tissue integration. Another potential source of the fibroblasts in the grafts is transdifferentiation of macrophages, as has previously been reported to be a naturally occurring process both in physiological healing as well as fibrosis,<sup>[78,79]</sup> although this warrants further investigation.

This study has several limitations. The conclusions regarding the immunofluorescent stainings are primarily based on qualitative analysis. Reliable quantification of the fluorescent stainings was compromised by the high background signal from the (auto)fluorescent scaffold material. Moreover, since it is well known that macrophage M1-M2 classification is oversimplified and non-binary, we decided to only describe the immunofluorescent data qualitatively, in order to prevent misinterpretation of quantitative data. With respect to the material functionalization, we opted to focus on assessing functional readouts on the biological level. However, we could not characterize for how long the heparin and the IL-4 were retained on the scaffold material in vivo. Important considerations for heparinization technologies are the bonding method and the long-term function of the heparin, which should guarantee uniform heparinization and sustained in vivo heparin bioactivity.<sup>[80]</sup> In this study, we relied on the UPy-HBP presence and its premixing with the UPy-polymer prior to electrospinning for the subsequent heparin functionalization. However, the distribution and exposure of the UPy-HBP on the electrospun meshes as well as the homogeneity of the heparin coating could not be assessed. While an extensive investigation of the heparin influence on intimal hyperplasia was beyond the scope of this study, future characterization of the UPy-HBP and heparin distribution might help explaining these results and allow for a better comparison with the several heparinization technologies (and their mixed in vivo results) available to date. With respect to the in vivo model used, the maximum follow-up time of 3 months in this study did not allow for complete scaffold resorption. Longer follow-up times are warranted to evaluate long-term performance of the grafts and to assess whether tissue homeostasis is achieved upon complete resorption of the synthetic scaffold material. Finally, when designing new biomaterial strategies for the clinic, preclinical evaluation should include animal models that better represent the patient population. Success or failure of in situ tissue engineering depends heavily on the regenerative potential of the patient.<sup>[81]</sup> This animal study was performed in healthy male rats with healthy vasculature, which lacks the persistent inflammatory environment often seen in patients requiring vascular grafts. Besides healthy versus diseased environments, also the influence of age and sex on the immune response and tissue regeneration should be taken into account, as well as larger animal models that more closely resemble the human pathology.<sup>[81]</sup>

Despite these limitations, the systematic comparison between the functionalization groups at both early and late timepoints in the inflammatory and healing cascade, and the unique use of Raman microspectroscopy, provides important added value to the field of vascular in situ tissue engineering. Particularly, the findings of this study extend the in-depth knowledge on the downstream effects of early modulation of the inflammatory response on tissue maturation and graft resorption.

## 4. Conclusion

In this study, we investigated the regenerative capacity of resorbable supramolecular vascular grafts, which were dual-functionalized with heparin and IL-4 to prevent thrombosis and modulate the inflammatory response to a pro-regenerative environment, respectively. The main findings are that, while thrombus formation was not a significant factor in any of the grafts, heparin-only functionalization led to adverse tissue formation in several cases, characterized by local intimal hyperplasia and disorganized (tropo)elastin formation. This was negated with the addition of IL-4, which showed more effective modulation of macrophage phenotype into a pro-regenerative M2 phenotype within the first week of implantation, and more organized tissue regeneration downstream and formation of more stable ECM. Importantly, variability between grafts was observed within each group, which warrants attention for future clinical translation. Taken together, this study contributes to our understanding of in situ vascular tissue regeneration and demonstrates that modulation of the early inflammatory response by dual functionalization aids as an effective tool to control endogenous tissue formation.

## 5. Experimental Section

**Peptide Synthesis:** The UPy-HBP peptide (GLRKKLGKA) was manually synthesized by Fmoc solid phase peptide synthesis methods, and coupling of the UPy-moiety on the resin.<sup>[23,82]</sup> The preparation of the supramolecular UPy-modified chain-extended polycaprolactone (CE-UPy-PCL;  $M_n = 19.3 \text{ kg mol}^{-1}$ ,  $M_w = 44.9 \text{ kg mol}^{-1}$ ) mixed with a UPy-modified heparin binding peptide (UPy-HBP) (Figure 1A,B) has been described in detail by Bonito et al.<sup>[23]</sup>

**Graft Preparation:** The CE-UPy-PCL was premixed with the UPy-HBP (0.5 mol%) and dissolved in chloroform ( $\text{CHCl}_3$ , Sigma) and hexafluoro-2-propanol (HFIP, Sigma) (15% w/v polymer in  $\text{CHCl}_3/\text{HFIP}$  80/20% v/v). After overnight stirring at room temperature, the polymer solution was used to fabricate isotropic electrospun tubular constructs. The solution was delivered at  $70 \mu\text{L min}^{-1}$  via a syringe pump (PHD 22/2000, Harvard Apparatus, Holliston, MA) to a charged moving needle (18 kV, 14 G) and collected on a rotating negatively charged  $\varnothing 2 \text{ mm}$  mandrel ( $-1 \text{ kV}$ , 2000 rpm) in a climate controlled ( $23 \text{ }^\circ\text{C}$ , 80% humidity) cabinet (IME Technologies, Geldrop, The Netherlands). The distance between the needle and the mandrel was kept constant at 17.5 cm. Afterwards, annealing of the electrospun tubes was performed for one week at  $37 \text{ }^\circ\text{C}$  to eliminate solvent remnants and to avoid polymer shrinkage. The scaffold microarchitecture (i.e., fiber diameter, morphology and organization) was assessed from SEM images (Quanta 600F, Thermo Fisher, Hillsboro, OR) (Figure 1C). The fiber diameter was assessed over 10 fibers per image ( $250\times$  magnification), with five images per scaffold. The overall wall thickness of the electrospun tubes was measured at 20 different locations using a digital microscope (VHX-500FE, Keyence, Mechelen, Belgium). To prevent transanastomotic cell ingrowth from adjacent native aorta an end-to-end anastomosis was made with a  $4 \times 10 \text{ mm}^2$  impenetrable Gore-Tex strip (internodal distance  $<1 \mu\text{m}$ ; Preclude Pericardial Membrane 1PCM103, Gore Medical) via 8–10 interrupted sutures and 2–3 mattress sutures (Ethilon 10-0, W2870, Ethicon) at both ends of the 8 mm length electrospun grafts (Figure 1D), as previously validated and described in detail.<sup>[18]</sup> The Gore-Tex sutured CE-UPy-PCL+UPy-HBP tubes were sterilized with Ethylene Oxide (Synergy Health, Venlo, The Netherlands).

**Suture Retention Test:** The suture retention strengths of the prepared tubes were measured according to ISO 7198 “Cardiovascular implants – Tubular vascular prostheses” using a tensile tester (CellScale, Canada) (Figure 1E). Briefly, 6 ethylene oxide sterilized grafts were tested; either with ( $n = 3$ ) or without ( $n = 3$ ) Gore-Tex strip. Samples were cut into 12 mm

long segments, fixed at one extremity by a clamp and pierced through at the other extremity by a 4-0 prolene suture (Ethicon, USA) at a distance of 2 mm from the edge. The tubes were stretched at 50 mm min<sup>-1</sup> until rupture in phosphate buffered saline (PBS) at 37 °C.

**Heparin/IL-4 Functionalization:** One day before surgery, the grafts were functionalized based on their experimental groups (Figure 1F) via incubation in the corresponding solutions overnight on a roller bank at 4 °C. The vascular grafts of the bare non-functionalized control group were incubated in Hank's balanced salt solution (HBSS) only. The heparin functionalized grafts were incubated in a solution of 20 ng mL<sup>-1</sup> of heparin sodium salt (Sigma-Aldrich, St. Louis, MO) in HBSS. For the heparin/IL-4 functionalized group, first 0.2 ng mL<sup>-1</sup> of rat recombinant IL-4 (400-04 Peprotech, Rocky Hill, NJ) was diluted in a 20 ng mL<sup>-1</sup> solution of heparin sodium salt in HBSS and allowed to premix for 30 min at 4 °C, after which the electrospun graft was placed in the solution for overnight incubation. Shortly before implantation, the grafts were rinsed in HBSS to remove unbound heparin and IL-4.

**Ethical Statement—In Vivo Study:** Study approval was obtained from the Animal Ethics Committee of the University of Utrecht (Instantie voor Dierenwelzijn, protocol number DEC-2013-108; 105134-1). All procedures were performed in accordance with and approved by the Institutional Animal Care and Use Committee of the University of Utrecht. Animal experiments were performed at the Central Lab Animal Research Facility of the University of Utrecht, The Netherlands. The study is reported in accordance with the Animal Research: Reporting In Vivo Experiments (ARRIVE) guidelines.<sup>[83]</sup>

**Animals and Housing:** Eighty-four healthy inbred specific pathogen free (SPF) male Lewis rats were purchased from Charles River (10–12 weeks old, 250–290 g). Each animal was fed ad libitum and housed in groups in cages with cage bedding and enrichment in an environment maintained at room temperature for 24 h a day and with a 12 h light–12 h dark cycle. The rats were carefully monitored for food intake, hind limb temperature, social behavior, and general physical condition and activity. The rats were randomly assigned into three different groups and follow-up time periods. Only male rats were chosen to avoid sex-related disturbances in immune cell expression and function due to hormone fluctuation.<sup>[84]</sup>

**Sample Size Calculations:** The sample size was calculated using the formula of L. Sachs

$$\eta = 2 \left( \frac{z_{\alpha}}{2} - 2\pi \right)^2 * \left( \frac{\sigma}{\delta} \right)^2 \quad (1)$$

$$F = 2 \left( \frac{z_{\alpha}}{2} - 2\pi \right)^2 \quad (2)$$

Based on previous data by Talacua et al., in which a bioactive molecule was added to an electrospun arterial graft in a similar rat model, it was hypothesized that the order of magnitudes of  $\delta$  and  $\sigma$  would be 15% and 10%, respectively.<sup>[18]</sup> With an  $\alpha$  of 0.05 and  $\pi$  of 80%, the sample size resulted in 7 animals/group. With 7 animals per condition, with four time-points and three different experimental groups a total of 84 animals were included in the study.

**Graft Implantation:** Vascular grafts were implanted as aorta interposition by using a previously described technique.<sup>[18]</sup> Briefly, all animals were examined by a veterinarian prior to surgery and were determined to be in good health. Before implantation of the graft, buprenorphine (Temgesic 0.05 mg kg<sup>-1</sup>, Schering Plough) was administered subcutaneously. Subsequently, animals were anesthetized with inhalation of isoflurane gas (induction 3–4%, maintenance 1.5–2.5%). Once adequate anesthesia was achieved, a midline laparotomy was performed and the abdominal viscera was lateralized for exposure of the abdominal aorta and the inferior vena cava. The aorta was separated from the inferior vena cava and the surrounding tissue. Subsequently, the segment of the abdominal aorta between the renal arteries and the aortic bifurcation was occluded using microvascular clamps. To prevent backflow, lumbar vessels originating from the aorta were ligated using single 10-0 sutures. The aorta was transected and the graft was sutured to the proximal and distal ends of the native aorta via 8–10 interrupted sutures (Figure 1G). After removal of the mi-

crovascular clamps, the pulsatile flow was confirmed in the aorta distal to the graft and the abdomen was closed. No heparin or other anticoagulants or antiplatelet drugs were administered during or after surgery. Maximum ischemia time was kept below 1 h. Animals recovered on heat pads to maintain adequate body temperature. Before rats returned to their cage, they were assessed for hind-limb paralysis or acute graft thrombosis. Postoperatively, animals received subcutaneous analgesia (buprenorphine 0.05 mg kg<sup>-1</sup>).<sup>[83]</sup>

**Graft Explanation:** Prior to sacrifice, rats underwent general physical examination to evaluate their condition. At termination, animals were anesthetized with inhalation of isoflurane gas (induction 3–4%, maintenance 1.5–2.5%). The abdomen was opened through the old incision. Microvascular clamps were re-positioned proximally and distally from the implanted tubes. The tubes were carefully explanted, dissected free from surrounding tissues, flushed with PBS and cut according to a predefined cutting scheme (Figure S1, Supporting Information) and stored in the appropriate solutions for analysis (Table S1, Supporting Information). Part of the native aorta was explanted and used as control tissue.

**General Histology:** Explanted grafts were fixed in 10% formalin overnight and embedded in paraffin. 5  $\mu$ m thick sections for histological analysis and 10  $\mu$ m thick sections for Raman measurements were cut using a microtome (Leica RM 2165, Leica microsystems) and transferred to poly-L-lysine coated glass slides (Thermo Fisher). The glass slides were dried in an oven at 37 °C and stored at room temperature. Before further processing, the slides were heated for 15 min at 60 °C and cooled down to room temperature. Tissue slides were deparaffinized in xylene (Merck) and dehydrated in graded series of ethanol. A modified Russell–Movat pentachrome stain (American MasterTech)<sup>[85]</sup> was performed to visualize overall tissue composition and organization. In addition, the slides were washed in acidified water (0.5% and 0.1% acetic acid). After staining, the slides were dehydrated and embedded in Entellan (Merck Serono).

**Immunohistochemistry:** Macrophages were stained using ED1+ (mouse anti-rat CD68, ab31630, 1:250; Abcam, Cambridge, UK). 5  $\mu$ m deparaffinized sections were first blocked with 5% hydrogen peroxide/PBS and subsequently subjected to indirect heat-induced antigen retrieval using either TRIS/EDTA, pH 9.0. After blocking with Superblock (Thermo Fischer Scientific, San Jose, CA, USA), the primary antibody was incubated for 1 h at room temperature. Sections were covered with eukitt after incubation with secondary horseradish peroxidase (HRP)-conjugated goat-antirabbit IgG (Brightvision Immunologic) visualization with Nova Red and hematoxylin counterstain.

**Immunofluorescence:** Before samples were stained, different antigen retrieval methods were performed, depending on the primary antibody used (Table S2, Supporting Information). For heat-mediated antigen retrieval, the tissue slides were washed twice in PBS and heated in a 96 °C water bath for 20 min in 1:10 citrate buffer (pH 6.1; Target Retrieval Solution, DAKO, Glostrup, Denmark). After heating, slides were slowly cooled down to room temperature for 45 min. For enzymatic antigen retrieval, 0.05% pepsin (Sigma) in 10  $\times$  10<sup>-3</sup> M hydrochloric acid (HCL) or 0.6 U mL<sup>-1</sup> Proteinase K (Sigma, in 50  $\times$  10<sup>-3</sup> M Tris Base, 1  $\times$  10<sup>-3</sup> M ethylene-di-amine-tetra-acetic acid (EDTA, ED2SS), 0.05% Triton X-100, pH 8.0) was applied to tissue slides for 12 min at a heat plate at 37 °C. Nonspecific binding was blocked with the blocking solution consisting of either 5% goat serum (Invitrogen) or 5% horse serum (Life Technologies) in 2% bovine serum albumin (BSA, Sigma) in PBS/0.05% Tween-20 (Merck Serono) for 2 h at room temperature in a humidified chamber. Primary antibodies were prepared in the optimized concentrations in 1:10 blocking solution. For the negative control, the samples were incubated with 1:10 diluted blocking solution only. Tissue slides were incubated overnight at 4 °C in a humidified chamber and then washed three times with PBS/Tween-20. The fluorescently labeled secondary antibody staining antibodies (vWF/vimentin/ $\alpha$ SMA, CD68/ELN, CD31) were diluted 1:500 in PBS/Tween-20. After incubation with the primary antibodies, the slides were washed in PBS/Tween-20 and incubated with the secondary antibodies for 1.5 h at room temperature in a humidified chamber. Directly after incubation with the secondary antibodies, the cell nuclei were counter stained with 4',6-diamidino-2-phenylindole (DAPI, Sigma) for 10 min at room temperature. Finally, the slides were washed three

times in PBS/Tween-20, and embedded in Mowiol (Sigma). For the antibody combination CD68/iNOS/Arg1 the primary antibody combination of CD68 and iNOS was performed first, followed by a blocking step with normal rabbit serum and subsequently incubated with the Arg1 antibody.

**Imaging:** Light microscopy images and tile scans were made using a bright field microscope (Zeiss Axio Observer Z1, 1 pixel = 0.27  $\mu\text{m}$  with a 40x/1.3NA Plan-Apochromat lens) and Zeiss ZEN software (version 3.2). The immunohistochemical CD68 staining was photographed on BX-51 microscope (Olympus, 1.25x magnification). To analyze macrophage positive area, NovaRed surface area in relation to total scaffold surface (%) was analyzed using ImageJ version 1.53 (National Institutes of Health, Bethesda, MD, USA). Fluorescent images and tile scans were recorded with a fluorescent microscope (Leica DMI8, 1 pixel = 0.65  $\mu\text{m}$  with a 20x/0.4 HC PL Fluotar lens), and further processed using Leica Application Suite X software (version 3.7, Leica Microsystems CMS GmbH).

**Raman Imaging and Spectral Analysis:** Confocal Raman microscopy and analysis were performed as described before.<sup>[29,86]</sup> In short, paraffin embedded 10  $\mu\text{m}$  slices of 3 month explants were imaged using a WITec alpha300 R Raman microscope equipped with a charge-coupled device (CCD) camera (WITec GmbH), a 532 nm laser, a 63x W Plan-Apochromat water dipping objective (N.A. 1.0 Carl Zeiss GmbH) and a spectrograph with a 600  $\text{g mm}^{-1}$  grating for spectral acquisition. First, a bright-field image was taken of the complete explant, then a representative area was chosen that included a transverse section of the vascular graft wall (covering adventitial tissue, degrading scaffold, matrix in between scaffold fibers and luminal tissue). Spectral mapping was performed at 2  $\mu\text{m}$  pixel resolution, an acquisition time of 0.05 s per spectrum and a laser power of 50 mW. Explanted native aorta, non-implanted ce-UPy-PCL+UPy-HBP were used as reference spectra. Spectral pre-processing and analysis were performed using Project FIVE 5.3 Plus software (WITec GmbH). The data sets were cropped (300–3050  $\text{cm}^{-1}$  wavenumbers), inspected for cosmic rays, background shape-corrected and normalized (area to 1) before performing TCA as also previously described.<sup>[86,87]</sup> TCA was used for the identification of components describing the distributions of synthetic material, collagen and actin rich regions across the spectral map. The data was then segmented based on the TCA results and 100 random single spectra were extracted using MATLAB (The MathWorks, Inc.).

Spectral differences were evaluated using PCA with Unscrambler X (CAMO Software AS). The spectral datasets were reduced in dimensionality via a vector-based approach. Each vector, called a PC, describes a source of variation within the data set. The first PC represents the highest contributing variation, the subsequent PCs refer to the next one and so on. PC values can be plotted against each other to visualize the correlation or separation of two or more data sets. Moreover, by using a pre calculated PCA model, new data can be projected into an existing model to be compared and categorized. PC score values and loadings were used to visualize and interpret molecular differences between native aortic ECM, the de novo ECM components (collagen and actin-rich) as well as the different scaffold resorption.

**Biochemical Assays:** DNA, GAG, HYP as a measure for collagen and ELN content were quantified from the explants. Prior to these assays, both wet weight and, after lyophilization overnight, dry weight was measured. After weighing, samples for DNA, GAG, HYP measurements were transferred to Nalgene cryogenic vials (Thermo Scientific, 5000-0012) containing  $\varnothing$  3 mm beads (Santorius, Goettingen, Germany), snap frozen in liquid nitrogen and disrupted to a fine powder using a micro-dismembrator (3  $\times$  30 s at 3000 rpm, Sartorius, Goettingen, Germany). After disruption, 500  $\mu\text{L}$  papain-enriched digestion buffer (100  $\times$  10<sup>-3</sup> M phosphate buffer (pH 6.5), 5  $\times$  10<sup>-3</sup> M L-cysteine (C1276, Sigma), 5  $\times$  10<sup>-3</sup> M ethylenediamine-tetra-acetic acid (EDTA, ED2SS, Sigma), and 140  $\mu\text{g mL}^{-1}$  papain (P4762, Sigma) was added, and the suspensions were transferred to new Eppendorf tubes for overnight digestion (16 h at 60 °C). Following digestion, samples were vortexed and centrifuged at 12 000 rpm for 10 min to precipitate scaffold remnants. The supernatant was used for DNA, GAG and HYP quantification. DNA content was quantified employing the Qubit dsDNA Broad Range Assay Kit (ThermoFisher Scientific) and the Qubit Fluorometer (ThermoFisher Scientific) according to the manufacturer's description. GAG quantities were determined with dimethyl methylene blue

(DMMB, Aldrich)<sup>[88]</sup> Shark chondroitin sulfate (C4348, Sigma) was included as a standard. In short, 40  $\mu\text{L}$  of the supernatants and prepared standards were pipetted in duplo in a 96-well plate. Subsequently, 150  $\mu\text{L}$  DMMB solution was added and absorbance was measured at 540 nm and 595 nm using a microplate reader (Synergy HT, BioTek). To quantify HYP content, digested samples were first hydrolyzed using 16 M hydroxide (B1438798, Merck). Then, HYP content was quantified with a Chloramin-T assay, including trans-4-hydroxyproline as a reference (H5534, Sigma).<sup>[89]</sup> Absorbance was measured at a wavelength of 550 nm. DNA, GAG and HYP contents were normalized to total dry mass to assess overall tissue formation. Following tissue extraction via oxalic acid, soluble  $\alpha$ -elastin was quantified via Fastin elastin assay (Biocolor Ltd), according to the manufacturer's protocol. ELN contents were normalized for the wet weight of the scaffolds.

**Mechanical Characterization:** Mechanical properties of both non-implanted scaffolds and explanted grafts were analyzed in PBS at 37° in a uniaxial tensile setup (CellScale Biomaterial Testing, Waterloo, Canada; equipped with a 1500 mN load cell) using LabJoy software (V8.01, CellScale Biomaterial Testing, Waterloo, Canada). The construct length and thickness were measured at 20 locations using a digital microscope (VHX-500FE, Keyence). Thereafter, the samples were mounted in the biorakes (tine diameter 245  $\mu\text{m}$ , puncture depth 1.9 mm, CS-BT-BR-07 World Precision Instruments). The ring shaped explants were mounted and tested until break at a constant speed of 10  $\text{mm min}^{-1}$  crosshead speed until failure, and the associated forces and displacements were recorded at a frequency of 5 Hz. The data was analyzed using an image-based approach developed by Van Haaften et al.<sup>[90]</sup> Briefly, the stretch outer perimeter  $\lambda_{\text{OP}}$  is defined as the outer parameter length normalized to the initial outer perimeter length, calculated from the image analysis. The estimated ring stress  $\sigma_{\text{ring}}$  was derived from the force and displacement measurements as previously described.<sup>[90]</sup>

**Scanning Electron Microscopy (SEM):** Explants analyzed for scaffold resorption were rinsed in purified water and decellularized with 4.6% sodium hypochlorite for 15 min at room temperature, followed by two washing steps in purified water, dried in vacuum overnight. Samples were visualized with SEM (low vacuum, 10 kV electron beam) (Quanta 600F; Thermo Fisher).

**Statistical Analysis:** Pre-processing of data was applied for biochemical assays, in which the data was normalized against dry weight (for DNA) of DNA (for GAG and HYP) or wet weight (for ELN). Sample size ( $n$ ) for each timepoint per experimental group are given in Table 1. Data are expressed as mean  $\pm$  SD. Normality of the data was assessed by plotting the frequency distribution and by performing the Shapiro Wilk test. When the data was normally distributed, statistical differences were determined using the two-way ANOVA with a Tukey's multiple comparison test. When the data was not normally distributed, the non-parametric Kruskal Wallis test with a Dunn's multiple comparison test were performed to identify statistical differences over time or between material types. Differences were considered as statistically significant for  $p$ -values below 0.05 and visualized with \* $p < 0.05$ , \*\* $p < 0.01$ , and \*\*\* $p < 0.001$ . Statistical analysis was performed using Prism software 8.0 (GraphPad Software, La Jolla, CA).

## Supporting Information

Supporting Information is available from the Wiley Online Library or from the author.

## Acknowledgements

V.B., S.K., A.S., and C.B. contributed equally to this work. The authors gratefully acknowledge Josephine Hermans, Agnes Barentsen, Harry Blom, Anja van der Sar, Rika Kramer, and Esmée Bouma of the Central Lab Animal Research Facility of the University of Utrecht, for facilitating and conducting the animal surgeries. Rogier Veltrop is gratefully acknowledged for his help with the collection of the explants, Bente de Kort for the elastin biochemical assays, Eline van Haaften, Marjan Hagelaars

and Rob Driessen for their help with the analysis of the uniaxial tensile tests, Annick Meeuwse for her help with the immunofluorescent imaging, and Krista den Ouden and Melanie Nieuwenhuijzen-van de Kaa for their expert technical assistance on the immunohistochemical stainings and analyses. The authors thank the ICMS animation studio for the schematic representation of the supramolecular polymers. This research is part of the ImaValve Project, which received funding from the European Union's Seventh Framework Programme (604514) and the InSiTeVx project (436001003), financially supported by ZonMw within the LSH 2Treat Programme and the Dutch Kidney Foundation. The collaboration between Eindhoven University of Technology and the University of Tübingen for the Raman spectroscopy analysis was facilitated by a Short-Term Fellowship (8169) of the European Molecular Biology Organization (EMBO) to Anthal Smits. The authors gratefully acknowledge the Gravitation Program "Materials Driven Regeneration," funded by the Netherlands Organization for Scientific Research (024.003.013).

## Conflict of Interest

The authors declare no conflict of interest.

## Data Availability Statement

Research data are not shared.

## Keywords

biodegradable polymers, cardiovascular, immunomodulatory biomaterials, in situ tissue engineering, Raman microspectroscopy, supramolecular chemistry, tissue-engineered vascular graft (TEVG)

Received: June 6, 2021

Revised: August 12, 2021

Published online: September 14, 2021

- [1] C. S. Ong, X. Zhou, C. Y. Huang, T. Fukunishi, H. Zhang, N. Hibino, *Expert Rev. Med. Devices* **2017**, *14*, 383.
- [2] M. Carrabba, P. Madeddu, *Front. Bioeng. Biotechnol.* **2018**, *6*, 41.
- [3] S. Li, D. Sengupta, S. Chien, *Wiley Interdiscip. Rev.: Syst. Biol. Med.* **2014**, *6*, 61.
- [4] D. G. Seifu, A. Purnama, K. Mequanint, D. Mantovani, *Nat. Rev. Cardiol.* **2013**, *10*, 410.
- [5] J. Chlupáč, E. Filová, L. Bacáková, *Physiol. Res.* **2009**, *58*, S119.
- [6] M. Desai, A. M. Seifalian, G. Hamilton, *Eur. J. Cardio-Thoracic Surg.* **2011**, *40*, 394.
- [7] I. Skovrind, E. B. Harvald, H. Juul Belling, C. D. Jørgensen, J. S. Lindholt, D. C. Andersen, *Stem Cells Transl. Med.* **2019**, *8*, 671.
- [8] Z. Wang, S. M. Mithieux, A. S. Weiss, *Adv. Healthcare Mater.* **2019**, *8*, 1900724.
- [9] H. P. Greisler, *Arch. Surg.* **1982**, *117*, 1425.
- [10] M. Zhu, Y. Wu, W. Li, X. Dong, H. Chang, K. Wang, P. Wu, J. Zhang, G. Fan, L. Wang, J. Liu, H. Wang, D. Kong, *Biomaterials* **2018**, *183*, 306.
- [11] T. Fukunishi, C. A. Best, T. Sugiura, J. Opfermann, C. S. Ong, T. Shinoka, C. K. Breuer, A. Krieger, J. Johnson, N. Hibino, *J. Thorac. Cardiovasc. Surg.* **2017**, *153*, 924.
- [12] L. A. Bockeria, O. Svanidze, A. Kim, K. Shatalov, V. Makarenko, M. Cox, T. Carrel, *J. Thorac. Cardiovasc. Surg.* **2017**, *153*, 1542.
- [13] T. B. Wissing, V. Bonito, C. V. C. Bouten, A. I. P. M. Smits, *npj Regen. Med.* **2017**, *2*, 18.
- [14] R. Duijvelshoff, A. di Luca, E. E. van Haften, S. Dekker, S. H. M. Söntjens, H. M. Janssen, A. I. P. M. Smits, P. Y. W. Dankers, C. V. C. Bouten, *Tissue Engineering Part A* **2021**, *27*, 894.
- [15] J. W. Reinhardt, J. de, D. R. Rosado, J. C. Barker, Y.-U. Lee, C. A. Best, T. Yi, Q. Zeng, S. Partida-Sanchez, T. Shinoka, C. K. Breuer, *Regener. Med.* **2019**, *14*, 389.
- [16] J. D. Roh, R. Sawh-Martinez, M. P. Brennan, S. M. Jay, L. Devine, D. a Rao, T. Yi, T. L. Mirensky, A. Nalbandian, B. Udelsman, N. Hibino, T. Shinoka, W. M. Saltzman, E. Snyder, T. R. Kyriakides, J. S. Pober, C. K. Breuer, *Proc. Natl. Acad. Sci. U. S. A.* **2010**, *107*, 4669.
- [17] N. Hibino, G. Villalona, N. Pietris, D. R. Duncan, A. Schoffner, J. D. Roh, T. Yi, L. W. Dobrucki, D. Mejias, R. Sawh-Martinez, J. K. Harrington, A. Sinusas, D. S. Krause, T. Kyriakides, W. M. Saltzman, J. S. Pober, T. Shin'oka, C. K. Breuer, *FASEB J.* **2011**, *25*, 2731.
- [18] H. Talacia, A. I. P. M. Smits, D. E. P. Muylaert, J. W. van Rijswijk, A. Vink, M. C. Verhaar, A. Driessen-Mol, L. A. van Herwerden, C. V. C. V. C. Bouten, J. Kluin, F. P. T. Baaijens, *Tissue Eng., Part A* **2015**, *21*, 2583.
- [19] N. Hibino, D. Mejias, N. Pietris, E. Dean, T. Yi, C. Best, T. Shinoka, C. Breuer, *FASEB J.* **2015**, *29*, 2431.
- [20] C. E. Witherel, D. Abebayehu, T. H. Barker, K. L. Spiller, *Adv. Healthcare Mater.* **2019**, *8*, 1801451.
- [21] A. Fernández-Colino, L. Iop, M. S. Ventura Ferreira, P. Mela, *Adv. Drug Delivery Rev.* **2019**, *146*, 17.
- [22] B. N. Brown, R. Londono, S. Tottey, L. Zhang, K. A. Kukla, M. T. Wolf, K. A. Daly, J. E. Reing, S. F. Badylak, *Acta Biomater.* **2012**, *8*, 978.
- [23] V. Bonito, A. I. P. M. Smits, O. J. G. M. Goor, B. D. Ippel, A. Driessen-Mol, T. J. A. G. Münker, A. W. Bosman, T. Mes, P. Y. W. Dankers, C. V. C. Bouten, *Acta Biomater.* **2018**, *71*, 247.
- [24] K. Sadtler, K. Estrellas, B. W. Allen, M. T. Wolf, H. Fan, A. J. Tam, C. H. Patel, B. S. Luber, H. Wang, K. R. Wagner, J. D. Powell, F. Housseau, D. M. Pardoll, J. H. Elisseeff, *Science* **2016**, *352*, 366.
- [25] I. S. Junttila, *Frontiers in Immunology* **2018**, *9*, <https://doi.org/10.3389/fimmu.2018.00888>.
- [26] E. den Dekker, S. Grefte, T. Huijs, G. B. ten Dam, E. M. M. Versteeg, L. C. J. van den Berk, B. A. Bladergroen, T. H. van Kuppevelt, C. G. Figdor, R. Torensma, *J. Immunol.* **2008**, *180*, 3680.
- [27] H. Lortat-Jacob, P. Garrone, J. Banchereau, J. a Grimaud, *Cytokine* **1997**, *9*, 101.
- [28] M. Votteler, D. A. Carvajal Berrio, M. Pudlas, H. Walles, U. A. Stock, K. Schenke-Layland, *J. Biophotonics* **2012**, *5*, 47.
- [29] J. Marzi, E. M. Brauchle, K. Schenke-Layland, M. W. Rolle, *Acta Biomater.* **2019**, *89*, 193.
- [30] S. Hinderer, E. Brauchle, K. Schenke-Layland, *Adv. Healthcare Mater.* **2015**, *4*, 2326.
- [31] B. G. Frushour, J. L. Koenig, *Biopolymers* **1975**, *14*, 379.
- [32] T. T. Nguyen, C. Gobinet, J. Feru, S. B. B. Pasco, M. Manfait, O. Piot, *Spectroscopy: An International Journal* **2012**, *27*, 421.
- [33] A. Y. F. You, M. S. Bergholt, J.-P. St-Pierre, W. Kit-Anan, I. J. Pence, A. H. Chester, M. H. Yacoub, S. Bertazzo, M. M. Stevens, *Sci. Adv.* **2017**, *3*, e1701156.
- [34] H. P. Buschman, G. Deinum, J. T. Motz, M. Fitzmaurice, J. R. Kramer, A. van der Laarse, A. V. Brusckhe, M. S. Feld, *Cardiovasc. Pathol.* **2001**, *10*, 69.
- [35] H. Ye, U. K. Rahul, T. Wang, S. Shi, J. Norfleet, S. De, *Sci. Rep.* **2019**, *9*, 19138.
- [36] A. P. Kotula, C. R. Snyder, K. B. Migler, *Polymer* **2017**, *117*, 1.
- [37] M. C. P. Brugmans, S. H. M. Sontjens, M. a. J. Cox, A. Nandakumar, A. W. Bosman, T. Mes, H. M. Janssen, C. V. C. Bouten, F. P. T. Baaijens, A. Driessen-Mol, *Acta Biomater.* **2015**, *27*, 21.
- [38] E. S. Fioretta, J. O. Fledderus, E. A. Burakowska-Meise, F. P. T. Baaijens, M. C. Verhaar, C. V. C. Bouten, *Macromol. Biosci.* **2012**, *12*, 577.
- [39] M. G. M. C. Mori da Cunha, B. Arts, L. Hympanova, R. Rynkevic, K. Mackova, A. W. Bosman, P. Y. W. Dankers, J. Deprest, *Acta Biomater.* **2020**, *106*, 82.
- [40] D. E. P. Muylaert, G. C. van Almen, H. Talacia, J. O. Fledderus, J. Kluin, S. I. S. Hendrikse, J. L. J. van Dongen, E. Sijbesma, A.

- W. Bosman, T. Mes, S. H. Thakkar, A. I. P. M. Smits, C. V. C. Bouten, P. Y. W. Dankers, M. C. Verhaar, *Biomaterials* **2016**, *76*, 187.
- [41] G. C. van Almen, H. Talacua, B. D. Ippel, B. B. Mollet, M. Ramaekers, M. Simonet, A. I. P. M. Smits, C. V. C. V. C. Bouten, J. Kluin, P. Y. W. Dankers, *Macromol. Biosci.* **2016**, *16*, 350.
- [42] B. J. De Kort, J. Marzi, E. E. Brauchle, A. M. Lichauco, H. Bauer, A. Serrero, S. Dekker, M. A. Cox, F. Schoen, K. Schenke-Layland, C. V. C. Bouten, A. I. P. M. Smits, *BioRxiv* 2021, <https://doi.org/10.1101/2021.04.06.438611>
- [43] M. Uiterwijk, A. I. P. M. Smits, D. van Geemen, B. van Klarenbosch, S. Dekker, M. J. Cramer, J. W. van Rijswijk, E. B. Lurier, A. Di Luca, M. C. P. Brugmans, T. Mes, A. W. Bosman, E. Aikawa, P. F. Gründerman, C. V. C. Bouten, J. Kluin, *JACC Basic Transl. Sci.* **2020**, *5*, 1187.
- [44] D. L. Morales, C. Herrington, E. A. Bacha, V. O. Morell, Z. Prodán, T. Mroczek, S. Sivalingam, M. Cox, G. Bennink, F. M. Asch, *Frontiers in Cardiovascular Medicine* **2021**, *7*, <https://doi.org/10.3389/fcvm.2020.583360>.
- [45] B. H. Walpoth, R. Rogulenko, E. Tikhvinskaia, S. Gogolewski, T. Schaffner, O. M. Hess, U. Althaus, *Circulation* **1998**, *98*, I1319.
- [46] R. R. R. Janairo, J. J. D. Henry, B. L.-P. Lee, C. K. Hashi, N. Derugin, R. Lee, S. Li, *IEEE Trans. Nanobiosci.* **2012**, *11*, 22.
- [47] X. Hui, X. Geng, L. Jia, Z. Xu, L. Ye, Y. Gu, A. - Y. Zhang, Z. - G. Feng, *J. Biomater. Appl.* **2020**, *34*, 812.
- [48] W. S. Choi, Y. K. Joung, J. W. Bae, H. K. Park, Y. H. Park, J. C. Park, K. D. Park, *ACS Appl. Mater. Interfaces* **2016**, *8*, 4336.
- [49] D. L. Gardner, W. V. Sharp, K. L. Ewing, A. F. Finelli, *Trans. Am. Soc. Artif. Int. Organs* **1969**, *15*, 7.
- [50] Y. Matsuzaki, R. Iwaki, J. W. Reinhardt, Y.-C. Chang, S. Miyamoto, J. Kelly, J. Zbinden, K. Blum, G. Mirhaidari, A. Ulziibayar, T. Shoji, C. K. Breuer, T. Shinoka, *Acta Biomater.* **2020**, *115*, 176.
- [51] Y. Wei, Y. Wu, R. Zhao, K. Zhang, A. C. Midgley, D. Kong, Z. Li, Q. Zhao, *Biomaterials* **2019**, *204*, 13.
- [52] B. Jiang, R. Suen, J. J. Wang, Z. J. Zhang, J. A. Wertheim, G. A. Ameer, *Adv. Healthcare Mater.* **2016**, *5*, 1594.
- [53] M. T. Koobatian, S. Row, R. J. Smith, C. Koenigsnecht, S. T. Andreadis, D. D. Swartz, *Biomaterials* **2016**, *76*, 344.
- [54] R. J. Smith, T. Yi, B. Nasiri, C. K. Breuer, S. T. Andreadis, *FASEB J.* **2019**, *33*, 5089.
- [55] I. Björk, U. Lindahl, *Mol. Cell. Biochem.* **1982**, *48*, 161.
- [56] D. Bergqvist, N. Jensen, N. H. Persson, *Int. Angiol.* **1988**, *7*, 65.
- [57] T. Bârzu, M. Pascal, J. -M. Herbert, P. Carayon, A. Desmoulière, *J. Cell. Physiol.* **1994**, *160*, 239.
- [58] R. S. Navarro, L. Jiang, Y. Ouyang, J. Luo, Z. Liu, Y. Yang, P. Qiu, K. Kuroda, Y. E. Chen, P. X. Ma, B. Yang, *Biomaterials* **2021**, *184*, 120874.
- [59] Y. Matsuzaki, S. Miyamoto, H. Miyachi, R. Iwaki, T. Shoji, K. Blum, Y.-C. Chang, J. Kelly, J. W. Reinhardt, H. Nakayama, C. K. Breuer, T. Shinoka, *Ann. Thorac. Surg.* **2021**, *111*, 1234.
- [60] J. J. D. Henry, J. Yu, A. Wang, R. Lee, J. Fang, S. Li, *Biofabrication* **2017**, *9*, 035007.
- [61] Y. Feng, Q. Li, D. Wu, Y. Niu, C. Yang, L. Dong, C. Wang, *Biomaterials* **2017**, *134*, 128.
- [62] A. Abbadi, J. Loftis, A. Wang, M. Yu, Y. Wang, S. Shakya, X. Li, E. Maytin, V. Hascall, *J. Biol. Chem.* **2020**, *295*, 4849.
- [63] R. P. Tan, A. H. P. Chan, S. Wei, M. Santos, B. S. L. Lee, E. C. Filipe, B. Akhavan, M. M. Bilek, M. K. C. Ng, Y. Xiao, S. G. Wise, *JACC Basic Transl. Sci.* **2019**, *4*, 56.
- [64] V. A. Kumar, N. L. Taylor, S. Shi, N. C. Wickremasinghe, R. N. D'Souza, J. D. Hartgerink, *Biomaterials* **2015**, *52*, 71.
- [65] M. D. Swartzlander, C. A. Barnes, A. K. Blakney, J. L. Kaar, T. R. Kyriakides, S. J. Bryant, *Biomaterials* **2015**, *41*, 26.
- [66] C. L. Jenkins, L. E. Bretscher, I. A. Guzei, R. T. Raines, *J. Am. Chem. Soc.* **2003**, *125*, 6422.
- [67] R. Duijvelshoff, M. S. Cabrera, B. Sanders, S. Dekker, A. I. P. M. Smits, F. P. T. Baaijens, C. V. C. Bouten, *JACC Basic Transl. Sci.* **2020**, *5*, 1095.
- [68] S. Liu, A. Bajpai, E. A. Hawthorne, Y. Bae, P. Castagnino, J. Monslow, E. Puré, K. L. Spiller, R. K. Assoian, *JCI Insight* **2019**, *4*, <https://doi.org/10.1172/jci.insight.122742>.
- [69] E. E. van Haften, R. Duijvelshoff, B. D. Ippel, S. H. M. Söntjens, M. H. C. J. van Houtem, H. M. Janssen, A. I. P. M. Smits, N. A. Kurniawan, P. Y. W. Dankers, C. V. C. Bouten, *Acta Biomater.* **2019**, *92*, 48.
- [70] T. B. Wissing, V. Bonito, E. E. van Haften, M. van Doeselaar, M. M. C. P. Brugmans, H. M. Janssen, C. V. C. Bouten, A. I. P. M. Smits, *Front. Bioeng. Biotechnol.* **2019**, *7*, 87.
- [71] J. Kluin, H. Talacua, A. I. P. M. Smits, M. Y. Emmert, M. C. P. Brugmans, E. S. Fioretta, P. E. Dijkman, S. H. M. Söntjens, R. Duijvelshoff, S. Dekker, M. W. J. T. Janssen-van den Broek, V. Lintas, A. Vink, S. P. Hoerstrup, H. M. Janssen, P. Y. W. Dankers, F. P. T. Baaijens, C. V. C. Bouten, *Biomaterials* **2017**, *125*, 101.
- [72] R. Khosravi, K. S. Miller, C. A. Best, Y. C. Shih, Y.-U. Lee, T. Yi, T. Shinoka, C. K. Breuer, J. D. Humphrey, *Tissue Eng., Part A* **2015**, *21*, 1529.
- [73] H. Bergmeister, N. Seyidova, C. Schreiber, M. Strobl, C. Grasl, I. Walter, B. Messner, S. Baudis, S. Fröhlich, M. Marchetti-Deschmann, M. Grieser, M. Franco, M. Krssak, R. Liska, H. Schima, *Acta Biomater.* **2015**, *11*, 104.
- [74] K. Berger, L. R. Sauvage, A. M. Rao, S. J. Wood, *Ann. Surg.* **1972**, *175*, 118.
- [75] P. Zilla, D. Bezuidenhout, P. Human, *Biomaterials* **2007**, *28*, 5009.
- [76] T. Pennel, D. Bezuidenhout, J. Koehne, N. H. Davies, P. Zilla, *Acta Biomater.* **2018**, *65*, 237.
- [77] S. Tara, H. Kurobe, K. A. Rocco, M. W. Maxfield, C. A. Best, T. Yi, Y. Naito, C. K. Breuer, T. Shinoka, *Atherosclerosis* **2014**, *237*, 684.
- [78] X. - M. Meng, S. Wang, X. - R. Huang, C. Yang, J. Xiao, Y. Zhang, K. - F. To, D. J. Nikolic-Paterson, H. - Y. Lan, *Cell Death Dis.* **2016**, *7*, e2495.
- [79] N. Haider, L. Boscá, H. R. Zandbergen, J. C. Kovacic, N. Narula, S. González-Ramos, M. Fernandez-Velasco, S. Agrawal, M. Paz-García, S. Gupta, K. DeLeon-Pennell, V. Fuster, B. Ibañez, J. Narula, *J. Am. Coll. Cardiol.* **2019**, *74*, 3124.
- [80] P. C. Begovac, R. C. Thomson, J. L. Fisher, A. Hughson, A. Gällhagen, *Eur. J. Vasc. Endovasc. Surg.* **2003**, *25*, 432.
- [81] A. I. P. M. Smits, C. V. C. Bouten, *Curr. Opin. Biomed. Eng.* **2018**, *6*, 17.
- [82] P. Y. W. Dankers, I. de Feijter, O. J. G. M. Goor, S. I. S. Hendrikse, M. Comellas-Aragonès, S. H. M. Söntjens, S. Zaccaria, P. P. K. H. Franssen, J. W. Peeters, L.-G. Milroy, *Synlett* **2015**, *26*, 2707.
- [83] C. Kilkenny, W. J. Browne, I. C. Cuthill, M. Emerson, D. G. Altman, *PLoS Biol.* **2010**, *8*, e1000412.
- [84] S. L. Klein, K. L. Flanagan, *Nat. Rev. Immunol.* **2016**, *626*.
- [85] H. K. Russell, *Arch. Pathol.* **1972**, *94*, 187.
- [86] A. Zbinden, J. Marzi, K. Schlünder, C. Probst, M. Urbanczyk, S. Black, E. M. Brauchle, S. L. Layland, U. Kraushaar, G. Duffy, K. Schenke-Layland, P. Loskill, *Matrix Biol.* **2020**, *85–86*, 205.
- [87] A. Zbinden, S. L. Layland, M. Urbanczyk, D. A. Carvajal Berrio, J. Marzi, M. Zauner, A. Hammerschmidt, E. M. Brauchle, K. Sudrow, S. Fink, M. Templin, S. Liebscher, G. Klein, A. Deb, G. P. Duffy, G. M. Crooks, J. A. Eble, H. K. A. Mikkola, A. Nsair, M. Seifert, K. Schenke-Layland, *Advanced Science* **2021**, *8*, 2002500.
- [88] R. W. Farndale, D. J. Buttle, A. J. Barrett, *Biochim. Biophys. Acta* **1986**, *883*, 173.
- [89] G. Huszar, J. Maiocco, F. Naftolin, *Anal. Biochem.* **1980**, *105*, 424.
- [90] E. E. Van Haften, M. C. Van Turnhout, N. A. Kurniawan, *Soft Matter* **2019**, *15*, 3353.